

## Polymer nanofilms with enhanced microporosity by interfacial polymerisation

Maria F. Jimenez-Solomon<sup>1†</sup>, Qilei Song<sup>1†</sup>, Kim E. Jelfs<sup>2</sup>, Marta Munoz-Ibanez<sup>1</sup> and Andrew G. Livingston<sup>1\*</sup>

<sup>1</sup>Department of Chemical Engineering, Imperial College London, London SW7 2AZ, UK,

<sup>2</sup>Department of Chemistry, Imperial College London. London SW7 2AZ, UK.

<sup>†</sup>These authors contributed equally to this work.

\* e-mail: a.livingston@imperial.ac.uk

**Highly permeable and selective membranes are desirable for energy-efficient gas and liquid separations. Microporous organic polymers have attracted significant attention in this respect owing to their high porosity, permeability, and molecular selectivity. However, it remains challenging to fabricate selective polymer membranes with controlled microporosity which are stable in solvents. Here we report a new approach to designing crosslinked, rigid polymer nanofilms with enhanced microporosity by manipulating the molecular structure. Ultra-thin polyarylate nanofilms with thickness down to 20 nm were formed in-situ by interfacial polymerisation. Enhanced microporosity and higher interconnectivity of intermolecular network voids, as rationalised by molecular simulations, are achieved by utilising contorted monomers for the interfacial polymerisation. Composite membranes comprising polyarylate nanofilms with enhanced microporosity fabricated in-situ on crosslinked polyimide ultrafiltration membranes show outstanding separation performance in organic solvents, with up to two orders of magnitude higher solvent permeance than membranes fabricated with nanofilms made from non-contorted planar monomers.**

Conventional gas and liquid separation processes such as evaporation and distillation are widely used in the oil and gas, energy, chemical, and pharmaceutical industries, but are energy-intensive. An alternative to these processes is membrane separation technology, which typically consumes an order of magnitude less energy. To enable wider deployment of membrane technology, highly permeable membranes are required to process large volumes of gas or solvent using a viable membrane area over a feasible timeframe<sup>1-2</sup>. There are two main strategies being followed to this end. One is to design the polymer structure at the molecular level so as to provide greater interconnected microporosity<sup>3-10</sup>, whilst a second approach is to reduce the thickness of the separating layer to nanometre scale<sup>11-16</sup>.

Microporous organic materials with well-defined pore structure are excellent candidates for highly permeable and selective membranes<sup>1</sup>, such as metal-organic frameworks (MOFs) and porous coordination polymers (PCPs)<sup>17-18</sup>, covalent organic frameworks (COFs)<sup>19-20</sup>, and porous organic cages

(POCs)<sup>21-23</sup>. However, the fabrication of these crystalline solids to form defect-free membranes is technically challenging. Recent significant progress includes fabrication of MOFs to form selective membranes by secondary crystal growth<sup>24</sup>, assembly of MOF nanosheets<sup>15</sup>, interfacial synthesis<sup>25</sup>, or mixed matrix membranes<sup>10,26</sup>. By contrast, industrial membranes are dominated by solution processing of polymers and interfacial polymerisation, for example in producing polyamide desalination membranes. Notable examples of microporous polymers are polymers of intrinsic microporosity (PIMs)<sup>6-7,27-31</sup>. Owing to the shape and rigidity of the component monomers, the polymer chains have contorted, rigid backbones resulting in inefficient packing, creating interconnected voids of less than 2 nm which behave as micropores. Due to their solubility in common solvents, linear-type PIMs can be processed into thin films which are highly permeable and selective for gas separations<sup>32-33</sup>. However, it is this solubility in a range of solvents which restricts their applications in organic solvent nanofiltration (OSN)<sup>34-35</sup>. Several efforts to make these PIM thin films solvent resistant have been reported, including thermal oxidative crosslinking<sup>9</sup>, chemical crosslinking<sup>28</sup>, and blending with thermally reactive polymers<sup>34</sup>; however these approaches introduce further processing steps.

Efforts to achieve higher separation performance, particularly higher permeance, have also sought to create ever-thinner membranes, such as PIM-1 nanofilms<sup>36</sup>, and MOF nanosheets<sup>15</sup>. Unexpectedly, recent work has shown that decreasing the thickness of solution cast films of PIM-1 below 100 nm resulted in a decrease, rather than an increase, in heptane permeance<sup>36</sup>. This was attributed to structural relaxation of the polymer molecules in the thin films. This effect has also been observed in gas permeation<sup>37</sup>, and suggests that linear macromolecules may not be suitable for ultra-thin nanofilms. By contrast, for nanofilms comprising crosslinked polymer networks or carbon networks, solvent permeance continues to increase as thickness is reduced. Fabrication of free-standing ultra-thin nanofilm membranes using metal hydroxide nanostrands as sacrificial substrates<sup>38-39</sup> was recently extended to formation of crosslinked polyamide nanofilms by interfacial polymerisation followed by DMF activation<sup>11</sup>. The resulting highly permeable ultra-thin free-standing polyamide nanofilms offer superior performance to conventional filtration membranes; however, sophisticated nanoscale processing steps are required in their fabrication.

Previous work indicates that introducing rigid moieties into polyamide nanofilms with thickness of 100 nm made by interfacial polymerisation enhances nanofilm porosity<sup>40</sup>. Nanofiltration performance was demonstrated for removal of salts from water, but these polyamide membranes had defects, limiting their application to other molecular separations<sup>40</sup>.

Here we report a new synthetic approach to designing polymer nanofilm membranes with enhanced microporosity **without complex processing**. We employed interfacial polymerisation with contorted and non-contorted monomers to synthesise defect-free, highly crosslinked polyarylate nanofilms down to 20 nm in thickness directly on ultrafiltration (UF) supports. The nanofilms fabricated with contorted monomers exhibit higher microporosity and interconnectivity than those made from non-contorted monomers. This results in up to two orders of magnitude higher permeance for organic solvents, and higher adsorption for gases. We hypothesize that upon interfacial polymerisation, the contorted monomers are held in non-coplanar orientations by the network structure, enhancing interconnectivity of intermolecular voids. This hypothesis is supported by our experimental results and molecular simulations. This work demonstrates that interfacial synthesis using contorted monomers provides nanofilms with a wide range of solvent resistance, tuneable structural diversity and enhanced microporosity defined by the geometry of monomers.

### **Formation of polymer nanofilms**

**Polymer nanofilms were synthesised by interfacial polymerisation.** We selected the interfacial polymerisation technique because it gives highly cross-linked polymer nanofilms *in situ*, ensuring stability in organic solvents. This simple, reproducible, and easily controllable technique has been used for synthesis of polyamide membranes for applications in reverse osmosis desalination and organic solvent nanofiltration<sup>11,41</sup>, MOF capsules<sup>42</sup> and gas separation membranes<sup>25</sup>. Here, polyarylate (PAR) (aromatic polyester) nanofilms were formed by reacting a phenol with trimesoyl chloride (TMC) at the interface between two immiscible solutions (Fig. **1a,c**, and Supplementary Fig. 1). We used contorted phenols including spiro-structured 5,5',6,6'-tetrahydroxy-3,3,3',3'-tetramethylspirobisindane (TTsBI) and 9,9-bis(4-hydroxyphenyl)fluorene (BHPF) to form polyarylates with enhanced microporosity, and

selected dihydroxyanthraquinone (DHAQ), and 1,3-benzenediol (RES) with planar structures as non-contorted controls (Fig. **1a**, and Supplementary Fig. 2 and 3). The spiro-centre within TTSBI has an angle of 90°, so when it reacts with TMC the TTSBI units are held in non-coplanar orientation by the polymer network (Fig. **1b**), enhancing interconnectivity of network voids. The spiro-centre prohibits the efficient packing of polymer segments in the networks, leading to relatively higher free volume. Figure **1d** shows a three dimensional view of a modelled amorphous cell containing a porous PAR-TTSBI network. To exploit their rigidity, solvent stability and enhanced porosity, we synthesised PAR nanofilms directly on porous supports and used them as selective membranes for gas separations and organic solvent nanofiltration (Fig. **1e** and **1f**).

Polyarylate nanofilms with thickness down to 20 nm can be formed via interfacial polymerisation (Fig. **2a**), and were transferred onto anodised alumina supports, allowing clear imaging with scanning electron microscopy (SEM) (Supplementary Fig. 4). The nanofilm thickness can be tuned by varying the concentration of monomers (Supplementary Fig. 4 and 5). To study the morphology and bulk properties of each polyarylate, we synthesised PAR powders via interfacial polymerisation in a two phase mixed reactor with rigorous stirring (PAR-IP) (Supplementary Fig. 2), and in monophasic liquid reactions (PAR-MP) (Supplementary Fig. 3). Polymer solids made interfacially show film-like morphologies (Fig. **2b** and Supplementary Fig. 6), whereas powders from monophasic reactions show agglomerated particles (Supplementary Fig. 7). Their chemical structure as aromatic polyesters was validated using infrared spectroscopy (Supplementary Fig. 8). Wide-angle X-ray scattering (WAXS) patterns confirm that these polymers are essentially amorphous except for PAR-DHAQ made by interfacial polymerisation, which shows some crystalline peaks possibly due to crystallization of monomers (Supplementary Fig. 9). The lattice spacings in WAXS for PAR polymers correspond well with the level of microporosity observed in gas sorption and modelling. Thermal analysis of all powders revealed high-temperature stability, with decomposition temperature under nitrogen atmosphere above 400 °C (Supplementary Fig. 10).



Polyarylate nanofilms formed at the interface of organic/aqueous monomer solutions can be captured and supported on a porous support, for example, anodised alumina membrane discs (Fig. **2a,c,d**). An alternative (and more practical for scale-up) approach is to fabricate nanofilms directly on polymer support membranes. Nanofilm composite membranes for gas separations were prepared in-situ on poly(trimethylsilyl)propyne (PTMSP)/alumina supports via interfacial polymerisation of monomers sequentially spin-coated on the substrates. A thin film of PTMSP (50 nm) was coated as an intermediate layer to assist with PAR film formation. Cross-sectional SEM images show similar nanofilm thicknesses (~50 nm) for all PAR nanofilms made on PTMSP/alumina supports (PAR/PTMSP) (Fig. **2e**, and Supplementary Fig. 11), enabling comparison of their gas permeances. Nanofilm composite membranes for OSN were prepared directly on crosslinked P84 polyimide (PI) UF supports and their surface morphologies characterised using SEM and atomic force microscopy (AFM) (Supplementary Fig. 12). PAR-TTSBI made on crosslinked PI support (PAR-TTSBI/PI) shows a smooth surface (Fig. **2f,g**). Lack of contrast between PI supports and PAR nanofilms did not allow determination of the nanofilm thickness using SEM. Instead, we transferred a PAR-TTSBI/non-crosslinked PI (nPI) nanofilm in a flipped configuration onto a silicon wafer and dissolved the PI support<sup>11,43</sup>. We then scratched the nanofilm to reveal the wafer surface and measured the height from the silicon wafer to the nanofilm surface using AFM, giving a thickness of ~20 nm (Fig. **2h,i**). The thickness of these supported nanofilms is similar to that of freestanding PAR-TTSBI nanofilms formed at the organic/aqueous interface using the same monomer concentrations (Fig. **2a**). The Young's modulus of a 50-nm thick PAR-TTSBI/nPI nanofilm was estimated as 4.8 GPa through wrinkling-based measurements under compressive stress induced by an elastomer substrate (Supplementary Fig. 13 and Table 1). This is higher than values reported for PIM-1 films<sup>9</sup>, or smooth polyamides prepared via interfacial polymerisation<sup>11</sup>, confirming the robustness of the PAR nanofilms.

### **Organic solvent nanofiltration performance**

**Polyarylate nanofilms with enhanced microporosity show rapid solvent transport and high molecular selectivity.** The effects of using contorted monomers in PAR nanofilms on the selectivity

and solvent permeance of PAR/PI nanofilm composite membranes are presented in Fig. 3a. For all PAR/PI membranes we found that methanol (MeOH), with the lowest molar volume and highest solubility parameter due to dipole force ( $\delta_p$ ) (Supplementary Table 2), gave the highest permeance (Fig. **3a**, and Supplementary Table 3), followed by acetone, tetrahydrofuran (THF), and finally toluene. This suggests that molar volume and solvent polarity control solvent permeance. Crosslinked PI support is known to undergo physical aging and compaction with applied pressure<sup>11</sup>, causing a decrease in permeance for PAR/PI membranes of about 45% over the first 5 hours of nanofiltration until steady state is reached (Supplementary Fig. 14). All reported permeance data in this work has been collected after this steady state was established. We also tested the OSN performance of a free-standing PAR-BHPF nanofilm (200 nm thick) on an anodised alumina disc (Supplementary Fig. 14); no decreases in permeance over time were observed for any of the solvents, confirming that the decrease in permeance is attributable to the PI support. We were unable to prepare defect-free 20 nm thick freestanding nanofilms on alumina with areas large enough for filtration tests, and so could not measure permeance of thinner films in this way. The PAR/PI membranes made from contorted monomers (TTSBI, BHPF) show much higher permeances for all solvents compared to PAR/PI membranes made from non-contorted, planar monomers (DHAQ, RES). Particularly, the permeance of THF in PAR-TTSBI and PAR-BHPF is as high as  $4.0 \text{ L m}^{-2} \text{ h}^{-1} \text{ bar}^{-1}$ , which is 100 times higher than PAR/RES ( $0.04 \text{ L m}^{-2} \text{ h}^{-1} \text{ bar}^{-1}$ ). The rejection of dyes is higher for the PAR-RES/PI membrane, as shown by the photographs of dye solutions (an inset photograph in Fig. 3b, and Supplementary Fig. 15), and effectively the same for the PAR/PI membranes made with other monomers (Fig. **3b** and Supplementary Tables 4 and 5). Rejections of styrene oligomers of different molecular weights in different solvents (Fig. **3d** and **3e**, and Supplementary Fig. 16) are the same for all PAR/PI membranes. The dramatic increase in permeance for the nanofilm membranes with enhanced microporosity is attributed to contorted species within these PAR nanofilms, confirming our hypothesis. Figures **3c** and **3f** show Rose Bengal rejection versus isopropanol permeance, and  $\alpha$ -methyl styrene dimer rejection versus acetone permeance, respectively for our PAR/PI membranes and polymeric OSN membranes reported in literature<sup>2</sup>.

Compared to these previously reported membranes<sup>2</sup>, the PAR nanofilm composite membranes with enhanced microporosity from this work show outstanding solvent permeance at the same selectivity.

A comparison between the OSN performance of polyarylate nanofilms with enhanced microporosity and previously reported sub-10-nm polyamide nanofilms<sup>11</sup> is provided in Supplementary Table 6. For nanofilm composite membranes utilising crosslinked PI supports, the polyarylate nanofilms offer comparable or better permeance than the polyamide nanofilms formed using nanostrands. The nanofilms mounted on alumina supports are harder to compare directly as their thicknesses differ widely. We note that among the polyamide nanofilms it is uniquely the m-phenylenediamine (MPD) based nanofilms that exhibit increased effective area through crumpling, and that respond favourably to dimethylformamide (DMF) activation. MPD and TMC are conventional monomers for desalination membranes, and the exceptional performance of the nanofilms derives from the complex nanoscale fabrication. However, there are significant challenges around the scale-up of both nanostrand fabrication and DMF activation. In contrast our polyarylate nanofilms are produced in-situ on ultrafiltration support membranes using regular interfacial polymerisation techniques, and their high permeance is due to the non-conventional contorted monomers employed. This supports designing the molecular architecture of nanofilms, using a wide range of chemistries, as an attractive alternative to the use of complex processing steps, to produce high permeance membranes.

### **Microporosity of polyarylate networks**

**The microporosity of polyarylate networks was investigated by various gas sorption techniques.**

N<sub>2</sub> adsorption isotherms at 77 K show low amounts of adsorption (Fig. **4a**), with BET surface areas lower than 40 m<sup>2</sup> g<sup>-1</sup> even for PAR polymers made from contorted monomers (Supplementary Table 7). This suggests restricted access of N<sub>2</sub> molecules within the narrow micropores in these rigid polymer networks. Low nitrogen uptake has been previously reported for other microporous polymers<sup>44</sup>, so further investigation used adsorption of CO<sub>2</sub> at 273 K. CO<sub>2</sub> has a smaller kinetic diameter than N<sub>2</sub> (3.3 Å for CO<sub>2</sub> and 3.64 Å for N<sub>2</sub>), so it can access micropores that are inaccessible to N<sub>2</sub>. PAR-BHPF and PAR-TTBI have higher BET areas (Supplementary Table 7) and higher CO<sub>2</sub> sorption (Fig. **4b** and **4c**)

than PAR-DHAQ and PAR-RES, with a characteristically steep uptake at low relative pressure particularly for PAR-MP powders, corroborating the microporous nature of PAR powders made from contorted monomers. PAR-MP powders show higher CO<sub>2</sub> sorption (Fig. 4b) than PAR-IP powders (Fig. 4c), possibly due to entrapment of starting materials and solvents in-between films formed during interfacial polymerisation with rigorous stirring. The CO<sub>2</sub> adsorption isotherms were analysed with the Langmuir model, giving much higher specific surface area for polyarylate nanofilms made from contorted monomers (150-160 m<sup>2</sup> g<sup>-1</sup>) via monophasic reaction, compared to polyarylates made from non-contorted monomers (61 m<sup>2</sup> g<sup>-1</sup>).

**Selective gas transport in polyarylate nanofilms.** We prepared defect-free PAR nanofilms supported on PTMSP (PAR/PTMSP) and studied single gas permeations at 295 K with gas molecules of different kinetic diameters, including He (2.60 Å), H<sub>2</sub> (2.89 Å), CO<sub>2</sub> (3.3 Å), O<sub>2</sub> (3.46 Å), N<sub>2</sub> (3.64 Å), and CH<sub>4</sub> (3.8 Å). The intermediate thin layer of PTMSP ages (Supplementary Fig. 17). However, it still gives sufficiently high gas permeance that allows the measurement of intrinsic gas transport properties of the relatively dense PAR nanofilms. As shown in Fig. 4d, gas permeance for PAR/PTMSP membranes decreases as He>H<sub>2</sub>>CO<sub>2</sub>>O<sub>2</sub>>N<sub>2</sub>>CH<sub>4</sub>, suggesting a molecular sieving separation, consistent with the selective permeation of solvents. The PAR-RES nanofilms show much lower permeances for large gas molecules (e.g. N<sub>2</sub> and CH<sub>4</sub>), resulting in much higher selectivities of small gas molecules over larger ones (H<sub>2</sub>/N<sub>2</sub> and H<sub>2</sub>/CH<sub>4</sub> up to 100), as shown in Fig. 4e. The PTMSP thin film supported on alumina shows no selectivity for H<sub>2</sub>/CO<sub>2</sub>, confirming that H<sub>2</sub>/CO<sub>2</sub> selectivity for PAR/PTMSP membranes is due to the molecular sieving effect of the PAR nanofilms. Figure 4f shows a plot of H<sub>2</sub>/CO<sub>2</sub> selectivity versus the permeability of CO<sub>2</sub> for the PAR nanofilms, calculated based on the thickness of the PAR layer, along with the upper-bound limit of polymer membranes<sup>45</sup>, including the fast-growing family of PIM polymers<sup>46</sup>. PAR-TTSBI/PTMSP and PAR-BHPF/PTMSP membranes show higher selectivity compared to polymer membranes with similar H<sub>2</sub> permeability, placing them close to the upper bound.

**Amorphous polymer model generation.** To investigate the pore structures of PAR networks, we performed molecular simulations to generate realistic structural models and analyse their properties. The amorphous polymer models were generated using Polymatic<sup>47</sup>, a simulated polymerisation

algorithm. Details of the molecular simulation are given in the Methods (Supplementary Tables 7 and 8). We generated five models for each system to ensure adequate sampling and averaged the properties across them (Supplementary Figs. 18 and 19). Figure 5a shows the monomers with different geometry. The top row images in Fig. **5b** show interconnected and disconnected voids with respect to a probe with a radius of 0.85 Å. PAR-BHPF and PAR-TTSBI show mostly interconnected voids, confirming our hypothesis that using contorted monomers results in nanofilms with enhanced microporosity and interconnectivity. In contrast, PAR-DHAQ and PAR-RES show isolated voids, confirming their lower porosity. The bottom row images in Fig. **5b** show voids coloured with respect to the largest radius probe that can be inserted. In Supplementary Fig. 19, PAR-BHPF and PAR-TTSBI exhibit substantially more pore volume than the corresponding 3D models of PAR nanofilms made from planar monomers. Pore size distributions for each PAR polymer network were derived from these simulations, showing similar values. This is consistent with comparable gas permeance and experimental OSN results (Fig. **5b**). These pore sizes are much smaller than the diameters of the organic solvents used in this work, so in principle no solvent should be able to access them. However, high solvent permeances were observed for PAR membranes with enhanced microporosity, suggesting that the interconnectivity and pore size of PAR networks is enlarged in organic solvents due to swelling. Simulation and experimental results give relatively higher surface areas and lower densities (Fig. **5c**, and Supplementary Table 7) for PAR-BHPF and PAR-TTSBI, compared to PAR-DHAQ and PAR-RES networks.

## Conclusions and outlook

In summary, by using rigid contorted monomers as building blocks for interfacial polymerisation, we have demonstrated the formation of ultrathin crosslinked polyarylate nanofilm membranes of enhanced microporosity. These membranes offer outstanding performance in organic solvent nanofiltration, where they are both more permeable and more selective than commercially available and previously reported membranes, showing high solvent permeance over a wide range of solvent polarity. The tuneable free volume of polyarylate networks in the solid state was confirmed by gas adsorption and permeation, and molecular dynamics simulation. The interfacial polymerisation process is used to produce reverse osmosis membranes for desalination that have revolutionized water purification

globally. Furthermore, crosslinked polyimide UF supports and the monomers used to form the polyarylate nanofilms are both commercially available, making up-scaling feasible. This work might inspire interfacial synthesis of the rapidly growing family of microporous polymers, such as PIMs, MOFs, COFs, and conjugated microporous polymers (CMPs), to obtain ultrathin microporous nanofilm based membranes with great potential for applications in molecular separations, including gas separation, organic solvent nanofiltration, water purification, and hydrocarbon separations in the petrochemical industry.

## References

1. Gin, D. L. & Noble, R. D., Designing the next generation of chemical separation membranes. *Science* **332**, 674-676 (2011).
2. Marchetti, P., Jimenez Solomon, M. F., Szekely, G., & Livingston, A. G., Molecular separation with organic solvent nanofiltration: A critical review. *Chemical Reviews* **114**, 10735-10806 (2014).
3. Guiver, M. D. & Lee, Y. M., Polymer rigidity improves microporous membranes. *Science* **339**, 284-285 (2013).
4. Freeman, B. D., Basis of permeability/selectivity tradeoff relations in polymeric gas separation membranes. *Macromolecules* **32**, 375-380 (1999).
5. Park, H. B. *et al.*, Polymers with cavities tuned for fast selective transport of small molecules and ions. *Science* **318**, 254-258 (2007).
6. Du, N. *et al.*, Polymer nanosieve membranes for CO<sub>2</sub>-capture applications. *Nat. Mater.* **10**, 372-375 (2011).
7. Carta, M. *et al.*, An efficient polymer molecular sieve for membrane gas separations. *Science* **339**, 303-307 (2013).
8. Song, Q. *et al.*, Photo-oxidative enhancement of polymeric molecular sieve membranes. *Nat. Commun.* **4**, 1918 (2013).
9. Song, Q. *et al.*, Controlled thermal oxidative crosslinking of polymers of intrinsic microporosity towards tunable molecular sieve membranes. *Nat. Commun.* **5**, 4813 (2014).
10. Rodenas, T. *et al.*, Metal-organic framework nanosheets in polymer composite materials for gas separation. *Nat. Mater.* **14**, 48-55 (2014).
11. Karan, S., Jiang, Z., & Livingston, A. G., Sub-10 nm polyamide nanofilms with ultrafast solvent transport for molecular separation. *Science* **348**, 1347-1351 (2015).
12. Karan, S. *et al.*, Ultrafast viscous permeation of organic solvents through diamond-like carbon nanosheets. *Science* **335**, 444-447 (2012).
13. Li, H. *et al.*, Ultrathin, molecular-sieving graphene oxide membranes for selective hydrogen separation. *Science* **342**, 95-98 (2013).
14. Nair, R. R. *et al.*, Unimpeded permeation of water through helium-leak-tight graphene-based membranes. *Science* **335**, 442-444 (2012).
15. Peng, Y. *et al.*, Metal-organic framework nanosheets as building blocks for molecular sieving membranes. *Science* **346**, 1356-1359 (2014).
16. Kim, H. W. *et al.*, Selective gas transport through few-layered graphene and graphene oxide membranes. *Science* **342**, 91-95 (2013).
17. Yaghi, O. M. *et al.*, Reticular synthesis and the design of new materials. *Nature* **423**, 705-714 (2003).

18. Kitagawa, S., Kitaura, R., & Noro, S.-i., Functional porous coordination polymers. *Angew. Chem., Int. Ed.* **43**, 2334-2375 (2004).
19. El-Kaderi, H. M. *et al.*, Designed synthesis of 3D covalent organic frameworks. *Science* **316**, 268-272 (2007).
20. Côté, A. P. *et al.*, Porous, crystalline, covalent organic frameworks. *Science* **310**, 1166-1170 (2005).
21. Jones, J. T. A. *et al.*, Modular and predictable assembly of porous organic molecular crystals. *Nature* **474**, 367-371 (2011).
22. Tozawa, T. *et al.*, Porous organic cages. *Nat. Mater.* **8**, 973-978 (2009).
23. Song, Q. *et al.*, Porous organic cage thin films and molecular-sieving membranes. *Adv. Mater.*, DOI: 10.1002/adma.201505688 (2016).
24. Li, Y. S. *et al.*, Controllable synthesis of metal-organic frameworks: From MOF nanorods to oriented MOF membranes. *Adv. Mater.* **22**, 3322-3326 (2010).
25. Brown, A. J. *et al.*, Interfacial microfluidic processing of metal-organic framework hollow fiber membranes. *Science* **345**, 72-75 (2014).
26. Dobrzańska, L., Lloyd, G. O., Esterhuysen, C., & Barbour, L. J., Guest-induced conformational switching in a single crystal. *Angew. Chem., Int. Ed.* **45**, 5856-5859 (2006).
27. McKeown, N. B. & Budd, P. M., Polymers of intrinsic microporosity (PIMs): Organic materials for membrane separations, heterogeneous catalysis and hydrogen storage. *Chem. Soc. Rev.* **35**, 675-683 (2006).
28. McKeown, N. B. *et al.*, Polymers of intrinsic microporosity (PIMs): Bridging the void between microporous and polymeric materials. *Chemistry - A European Journal* **11**, 2610-2620 (2005).
29. Carta, M. *et al.*, Triptycene induced enhancement of membrane gas selectivity for microporous Träger's base polymers. *Adv. Mater.* **26**, 3526-3531 (2014).
30. Ghanem, B. S., Swaidan, R., Litwiller, E., & Pinnau, I., Ultra-microporous triptycene-based polyimide membranes for high-performance gas separation. *Adv. Mater.* **26**, 3688-3692 (2014).
31. McKeown, N. B. & Budd, P. M., Exploitation of intrinsic microporosity in polymer-based materials. *Macromolecules* **43**, 5163-5176 (2010).
32. Budd, P. M. *et al.*, Solution-processed, organophilic membrane derived from a polymer of intrinsic microporosity. *Adv. Mater.* **16**, 456-459 (2004).
33. Budd, P. M. *et al.*, Gas separation membranes from polymers of intrinsic microporosity. *J. Membr. Sci.* **251**, 263-269 (2005).
34. Fritsch, D. *et al.*, High performance organic solvent nanofiltration membranes: Development and thorough testing of thin film composite membranes made of polymers of intrinsic microporosity (pims). *J. Membr. Sci.* **401-402**, 222-231 (2012).
35. Tsarkov, S. *et al.*, Solvent nanofiltration through high permeability glassy polymers: Effect of polymer and solute nature. *J. Membr. Sci.* **423-424**, 65-72 (2012).
36. Gorgojo, P. *et al.*, Ultrathin polymer films with intrinsic microporosity: Anomalous solvent permeation and high flux membranes. *Adv. Funct. Mater.* **24**, 4729-4737 (2014).
37. Murphy, T. M. *et al.*, Physical aging of layered glassy polymer films via gas permeability tracking. *Polymer* **52**, 6117-6125 (2011).
38. Ichinose, I., Kurashima, K., & Kunitake, T., Spontaneous formation of cadmium hydroxide nanostrands in water. *J. Am. Chem. Soc.* **126**, 7162-7163 (2004).
39. Karan, S. *et al.*, Ultrathin free-standing membranes from metal hydroxide nanostrands. *J. Membr. Sci.* **448**, 270-291 (2013).
40. Qian, H., Zheng, J., & Zhang, S., Preparation of microporous polyamide networks for carbon dioxide capture and nanofiltration. *Polymer* **54**, 557-564 (2013).

41. Jimenez Solomon, M. F., Bhole, Y., & Livingston, A. G., High flux membranes for organic solvent nanofiltration (OSN)—interfacial polymerization with solvent activation. *J. Membr. Sci.* **423–424**, 371-382 (2012).
42. Ameloot, R. *et al.*, Interfacial synthesis of hollow metal–organic framework capsules demonstrating selective permeability. *Nat Chem* **3**, 382-387 (2011).
43. Chung, J. Y., Lee, J.-H., Beers, K. L., & Stafford, C. M., Stiffness, strength, and ductility of nanoscale thin films and membranes: A combined wrinkling–cracking methodology. *Nano Lett.* **11**, 3361-3365 (2011).
44. Weber, J., Su, Q., Antonietti, M., & Thomas, A., Exploring polymers of intrinsic microporosity - microporous, soluble polyamide and polyimide. *Macromol. Rapid Commun.* **28**, 1871-1876 (2007).
45. Robeson, L. M., The upper bound revisited. *J. Membr. Sci.* **320**, 390-400 (2008).
46. Du, N., Park, H. B., Dal-Cin, M. M., & Guiver, M. D., Advances in high permeability polymeric membrane materials for CO<sub>2</sub> separations. *Energy Environ. Sci.* **5**, 7306-7322 (2012).
47. Abbott, L. J., Polymatic: A simulated polymerization algorithm; version 1.0; network for computational nanotechnology, Purdue University, West Lafayette, IN. <https://nanohub.org/resources/17278>. (2013).

## Acknowledgments

This work was financially supported by the Engineering and Physical Sciences Research Council (EPSRC, UK), 7th Framework Programme of the European Commission's Marie Curie Initiative, NEMOPUR Project (M.F.J.S.), Imperial College Junior Research Fellowship (Q.S.), and Royal Society University Research Fellowship (K.E.J.). The authors are grateful to P.R.J. Gaffney for assisting with monophasic reactions, and S. Karan for assisting with mechanical property measurements.

## Author contributions

M.F.J.S. and A.G.L. conceived the idea. M.F.J.S., Q.S. and A.G.L. designed the research. M.F.J.S. and Q.S. performed experiments, including synthesis of materials and membranes, and characterization analyses. M.F.J.S. carried out organic solvent nanofiltration. Q.S. performed gas permeation measurements. K.E.J. performed molecular dynamics simulations. M.M.I. assisted with synthesis of PAR/PI nanofilm composite membranes. M.F.J.S., Q.S. and A.G.L. wrote the manuscript. A.G.L. guided the project. All of the authors participated in the discussion and read the manuscript.

## Additional information

Supplementary information is available in the online version of the paper. Reprints and permissions information is available online at <http://www.nature.com/reprints>. Correspondence and requests for materials should be addressed to A.G.L.

## Competing financial interests

The authors declare no competing financial interests.

## Figure Captions

**Figure 1 | Interfacial synthesis of polyarylate nanofilms.** **a**, Synthesis of aromatic polyester (polyarylate) nanofilms via interfacial polymerisation. The aromatic phenol is dissolved in a dilute sodium hydroxide solution and reacts with trimesoyl chloride dissolved in hexane at the hexane/aqueous interface. Four different phenol monomers were used: spiro-structured 5,5',6,6'-tetrahydroxy-3,3',3',3'-tetramethylspirobisindane (TTSBI), cardo-structured 9,9-Bis(4-hydroxyphenyl)fluorene (BHPF), and planar structured 2,6-dihydroxyanthraquinone (DHAQ), and 1,3-benzenediol (RES). The cardo- and spiro-structured monomers are contorted, rigid monomers; DHAQ and RES are monomers with planar structures. **b**, Molecular model of a segment of polyarylate network containing spiro-contorted monomers from TTSBI. **c**, Visualization of the interfacial polymerisation between TMC in hexane and the phenoxide of TTSBI in aqueous NaOH solution. **d**, Three-dimensional view of an amorphous cell containing spiro-contorted TTSBI polyarylate network. Blue colour: surface at probe radius of 1 Å. Cell size: 46 x 46 x 46 Å. **e**, Schematic diagram of polyarylate nanofilm composite membrane used as a selective membrane for gas separations. **f**,



Schematic diagram of polyarylate nanofilm composite membrane used as a solvent-stable selective membrane for organic solvent nanofiltration (OSN).

**Figure 2 | Polyarylate nanofilms.** **a**, Cross-sectional SEM image of an ultra-thin free-standing polyarylate (TTSBI) nanofilm supported on porous alumina. The nanofilm was prepared by interfacial polymerisation of TTSBI (1 wt%) in NaOH/water with TMC (0.1 wt%) in hexane. Right inset: enlargement of the cross-section without tilting. **b**, SEM image of interfacially polymerised cardo-contorted polyarylate (BHPF) solids with nanofilm morphology, prepared by rigorous mixing of a solution of TMC in hexane added to a solution of BHPF in NaOH/water. **c**, A photograph of a thicker free-standing defect-free PAR-BHPF nanofilm supported on porous alumina support (diameter of 47 mm) held by tweezers. **d**, Cross-sectional SEM image of the PAR-BHPF nanofilm supported on porous alumina support. **e**, Cross-sectional SEM image of cardo-structured PAR-BHPF/PTMSP nanofilm supported on PTMSP/alumina. PAR nanofilms were prepared by sequential spin-coating of a solution of TMC in hexane and a solution of phenol in NaOH/water on PTMSP/alumina. Inset shows a photo of the nanofilm composite membrane (tested in gas permeation). **f**, SEM image of the surface of a PAR-TTSBI nanofilm interfacially polymerised on a crosslinked P84 polyimide membrane support. **g**, AFM image probed on the sample shown in (f). **h**, AFM image and (i) corresponding height profile of a section of a PAR-TTSBI nanofilm on top of a silicon wafer. A scratch was made to expose the wafer surface and allow measurement of the height from the silicon wafer surface to the upper nanofilm surface.

**Figure 3 | Organic solvent nanofiltration.** **a**, Pure solvent permeances for methanol (MeOH), acetone, tetrahydrofuran (THF), and toluene through polyarylate nanofilm composite membranes prepared on crosslinked polyimide supports. Nanofiltration was conducted in a cross-flow filtration system at 30°C under 30 bar. **b**, Rejection versus molecular weight of dyes: Brilliant Blue (BB, 826 g mol<sup>-1</sup>); Crystal Violet (CV, 408 g mol<sup>-1</sup>); Disperse Red (DR, 314 g mol<sup>-1</sup>); and Chrysoidine G (CSG, 249 g mol<sup>-1</sup>) in methanol. Inset photo shows the retentate (R, left) and permeate (P, right) samples for PAR-RES/PI. Nanofiltration was conducted separately for each dye in a cross-flow filtration system at 30°C under 30 bar. **c**, Isopropanol permeance versus the rejection of Rose Bengal (1017 g mol<sup>-1</sup>) for polyarylate/PI nanofilm composite membranes versus typical integrally skinned asymmetric (ISA), thin film composite (TFC), and thin film nanocomposite (TFN) membranes reported in the literature<sup>2</sup>. Nanofiltration was conducted in a dead-end stirred cell (500 rpm) at 30°C under 30 bar. **d,e**, Rejection versus the molecular weight of polystyrene oligomers for polyarylate/PI nanofilm composite membranes. Nanofiltration of a feed solution comprising polystyrene oligomers dissolved in acetone (**d**) or THF (**e**), respectively in a crossflow filtration system under 30 bar at 30°C. **f**, The permeance of acetone versus rejection of  $\alpha$ -methyl styrene dimer (236 g mol<sup>-1</sup>) for polyarylate/PI nanofilm composite membranes. Typical nanofiltration data of ISAs membranes, TFCs membranes, and TFNs membranes reported in the literature are included<sup>2</sup>. Based on the reported literature value, the upper bound line is manually added to show a trade-off between permeance of solvent and rejection of solute molecules.

**Figure 4 | Gas sorption and transport properties.** **a**, N<sub>2</sub> sorption at 77 K and **b**, CO<sub>2</sub> sorption at 273 K for polyarylate (PAR) networks prepared via interfacial polymerisation (IP). **c**, CO<sub>2</sub> sorption at 273 K for PAR networks synthesized via monophasic reaction. **d**, Gas permeance as a function of kinetic diameter of gas molecules through PAR nanofilm composite membranes supported on PTMSP thin films (50 nm) coated on alumina. Gas Permeation Unit (GPU): 1 GPU = 10<sup>-6</sup> cm<sup>3</sup> (STP) s<sup>-1</sup> cm<sup>-2</sup> cmHg<sup>-1</sup>. **e**, Ideal gas selectivity for typical gas pairs. **f**, Upper bound plot of H<sub>2</sub>/CO<sub>2</sub> selectivity versus permeability of H<sub>2</sub> for PAR nanofilms. [Permeability data are calculated based on the thickness of the PAR layer](#). Robeson's upper bound (2008) is plotted<sup>45</sup>. Commercial polymers are included for comparison: cellulose acetate (CA); ethyl cellulose (EC); Matrimid 5218 polyimide (PI); polyetherimide

(PEI); polyphenyleneoxide (PPO); polysulphone (PSF); poly(dimethylsiloxane) (PDMS). Typical high free volume PIM polymers (dark triangles) are included<sup>46</sup>.

**Figure 5 | Structural analysis of amorphous polymer models.** **a**, 3D molecular model of phenol monomers. **b**, *Top row* shows the interconnected (green) and disconnected (red) voids with respect to a probe of 0.85 Å radius - this is the largest size probe that can diffuse across any of the rigid models. These images highlight the difference between PAR-BHPF and PAR-TTSBI versus PAR-DHAQ and PAR-RES. *Bottom row* shows voids coloured with respect to the pore radius. Only voids that are larger than a radius of 1.42 Å (the kinetic radius of H<sub>2</sub>) are shown. **c**, Simulated pore size distributions averaged over 5 models for each of the polyarylate systems. **d**, Experimentally measured density of polyarylates prepared via interfacial polymerisation (PAR-IP) or via monophasic (PAR-MP) reaction versus simulated density values.

## Methods

**Synthesis of polymers.** Polyarylate solids were prepared by interfacial polymerisation or via monophasic reactions. Four different phenol monomers were used: contorted monomers including 5,5',6,6'-tetrahydroxy-3,3,3',3'-tetramethylspirobisindane (TTSBI, Alfa Aesar) and 9,9-Bis(4-hydroxyphenyl)fluorene (BHPF, Sigma Aldrich), and planar monomers including 2,6-Dihydroxyanthraquinone (DHAQ, Sigma Aldrich), and 1,3-benzenediol (resorcinol, RES, Sigma Aldrich). For interfacial polymerisation, each phenol monomer was dissolved in a diluted sodium hydroxide aqueous solution (pH=13) with a molar ratio of 4:1 (NaOH to TTSBI and BHPF), and 2:1 (NaOH to DHAQ and RES) (throughout this study), with concentrations of TTSBI (1 wt%), BHPF (1 wt%), DHAQ (2 wt%), and RES (2 wt%). The sodium phenoxides were then reacted interfacially with trimesoyl chloride (TMC, Sigma Aldrich) dissolved in hexane (0.2 wt % by volume) under rigorous stirring for 2 min. The resulting polymers were then washed thoroughly with water, followed by hexane. They were then freeze-dried from hexane and dried at 120 °C under vacuum for 12h. For monophasic polymerisation reactions, 1 g phenol was mixed with TMC at 1:1 molar ratio dissolved in dry degassed THF (40-60 mL). An 11-fold molar excess of dry pyridine was added through a syringe under nitrogen gas and stirring. After reflux for 20 h, a precipitate was formed, which was washed with 1M HCl solution, water and THF. It was subsequently dried via freeze drying, and then at 120 °C in a vacuum oven for 12 h.

**Synthesis of free-standing polymer nanofilms.** Free-standing PAR nanofilms were fabricated by interfacial polymerisation. Phenol monomers were dissolved in aqueous basic NaOH solutions with varied concentrations of TTSBI (1 wt%), BHPF (1 wt%), and RES (2 wt%). A solution of 0.1 % (w/v) TMC in hexane was slowly added to the aqueous solution, and allowed to react for 2 min. Afterwards, the resulting nanofilms were immediately withdrawn from the interface with a clean glass substrate, washed in clean distilled water, and transferred to an anodized aluminium oxide (AAO) membrane disc (Anodisc, Whatman) with a surface layer of 20 nm nanopores. To form a thicker nanofilm (200 nm) for solvent permeation studies, a 1 % (w/v) TMC in hexane solution was used and reacted with an aqueous solution of BHPF (1 wt%) in NaOH.

**Fabrication of ultrafiltration support membranes.** Cross-linked polyimide (PI) ultrafiltration (UF) support membranes were prepared and conditioned following the same methodology as previously reported by our group<sup>48</sup>. In brief, a polymer dope solution was prepared by dissolving 22 % (w/w) polyimide (P84) (HP Polymer GmbH, Austria) in DMSO and stirring overnight until complete dissolution. A viscous solution (2250 cP at 22 °C) was formed, and allowed to stand for 10 hours to remove air bubbles. The dope solution was then cast on the smooth side of a polypropylene nonwoven backing (Novatexx 2471, Freudenberg, Germany) at a casting speed of 0.035 ms<sup>-1</sup> using a Sepratek continuous casting machine with a casting knife set at a gap of 250 µm located in a room held at constant temperature (21 °C). Immediately after casting, the membrane was immersed in a deionized water bath at 21 °C where phase inversion occurred. After 15 min, membranes were transferred to a fresh water bath and left for an hour. The wet membranes were then immersed in an isopropanol exchange bath to remove any residual water and preparation solvents. The support membranes were cross-linked as described elsewhere<sup>48</sup>, by immersing the membrane in a solution of 1,6-hexanediamine (HAD, Sigma Aldrich) in isopropanol (120 g L<sup>-1</sup>) for 16 hours at room temperature. The membranes were then removed from the crosslinking bath and washed with isopropanol for 3 h to remove any residual HDA. The support membranes were conditioned with polyethylene glycol 400 (PEG 400, VWR) before the interfacial polymerisation reaction. The conditioning step involved immersing the membrane overnight in a conditioning agent bath comprising polyethylene glycol 400 in isopropanol at a volume ratio of 3:2. The membranes were then dried at room temperature inside a fume hood.

**Nanofilm composite membranes.** Nanofilm composite membranes for OSN were prepared by interfacial polymerisation directly on conditioned crosslinked polyimide (PI) P84 ultrafiltration (UF) supports using different monomers (see Supplementary Figure 2). Interfacial polymerisation to form polyarylate nanofilms was performed by exposing the surface of the UF support to an aqueous basic solution of sodium phenoxide, including TTSBI (1 wt%), BHPF (1 wt%), DHAQ (2 wt%) and RES (2 wt%) for 2 min. The phenoxide loaded support membranes were then pressed with a roller and air was applied to remove excess solution. The membranes were then exposed to TMC in hexane (0.1 % w/v) for 2 min. The resulting membranes were withdrawn from the hexane solution, dried in air, and cured in a ventilated oven at 85 °C for 10 min to complete crosslinking. The membranes were then stored in distilled water at 4 °C. As a control, a conditioned polyimide UF support was immersed in the aqueous and organic phases without monomers and cured in a ventilated oven under the same conditions (see Supplementary Figure 14).

Nanofilm composite membranes for gas permeation tests were prepared by *in situ* polymerisation of polyarylate nanofilms. First, a thin layer (about 50 nm) of poly(trimethylsilyl)propyne (PTMSP, Fluorochem, UK) was coated on the AAO alumina support (diameter of 25 mm) by spin-coating a PTMSP solution in chloroform (0.5 wt%) at 2000 rpm for 1 min. Then a drop of solution of TMC (1 wt%) in hexane was spin-coated on the alumina-PTMSP substrates at 2000 rpm for 1 min. Subsequently, a drop of phenoxide solution (1 wt%) in water was added to the surface and spin-coated at 2000 rpm for 1 min. *In situ* polymerisation occurs at the interface forming a thin polyarylate nanofilm.

**Characterization methods.** Fourier transform-Infrared spectra (FT-IR) were recorded on a Perkin-Elmer Spectrometer 100, with samples mounted on a zinc-selenium/diamond plate. Thermal analyses were performed with a thermogravimetric analyser (TGA) Q500 (TA Instruments, UK). Polymer powders were heated from room temperature to 900 °C at 10 °C min<sup>-1</sup> in N<sub>2</sub>. Densities of polymer solids were measured using a Micrometrics Accupyc 1340 helium pycnometer equipped with 5 cm<sup>3</sup> insert. The obtained values are the mean and standard deviation from a cycle of 10 measurements. Samples were evacuated thoroughly under vacuum at 120 °C for 24 h prior to measurements. Low-pressure gas sorption was performed using a Micrometrics TriStar or ASAP2050 surface area analyzer. Samples were dried at 120 °C under vacuum for 12 h, and then loaded into the apparatus and degassed at 120 °C for 12 h. Nitrogen adsorption isotherms were measured at 77 K and CO<sub>2</sub> sorption isotherms were measured at 273 K. Wide-angle X-ray scattering was performed with a Bruker D8 machine operated at 40 mA and 40 kV using Cu K $\alpha$  radiation with a step of 0.02° per second. SEM was carried out using a field emission gun scanning electron microscope (LEO 1525 from Karl Zeiss) or a Hitachi S5500 microscope. For cross-sectional SEM imaging, the polymer films were freeze-fractured in liquid nitrogen. Samples were sputter-coated with a thin layer of chromium or gold and palladium. AFM imaging was performed on a Veeco AFM Dimension 3100 equipped with a DAFMLN Dimension AFM scan head and a Nanoscope VI controller. Samples were attached to glass slides using a double sided tape. The scans were performed in an air medium. The images were scanned in tapping mode using silicone cantilevers having a nominal diameter of less than 10 nm. Scanning was performed at a speed of 1.3 Hz, and a scan size of 5  $\mu$ m was used for standard images. Bruker ‘NanoScope Analysis beta’ or ‘Gwyddion 2.38 SPM data visualization and analysis software’ were used to process the AFM images. Roughness was estimated from at least three images of the same membrane scanned over an area of 5  $\mu$ m  $\times$  5  $\mu$ m from each sample. To measure the thickness from AFM, polyarylate-TTSBI nanofilms were made on non-crosslinked PI support, so that the support could be dissolved and the nanofilm analysed on its own. Nanofilm composite membranes were transferred in a flipped configuration onto a silicon wafer and the polyimide support was dissolved. A scratch was made to expose the wafer surface. The thickness of the nanofilm was estimated from the height difference between the silicon and the upper surface of the nanofilm using a one dimensional statistical function. The mechanical properties of polyarylate nanofilms were measured using a wrinkle-based method,<sup>11,43,49</sup> by generating compressive stress in the nanofilms supported on stretched poly(dimethylsiloxane) (PDMS) strips (details are given in Supplementary Figure 13). The Young’s modulus are derived and presented in Supplementary Table 1.

**Organic solvent nanofiltration.** Nanofiltration performance was evaluated in terms of permeance of organic solvent and rejection of oligomers or dye molecules with varied molecular weights. Most nanofiltration experiments were carried out in repeats of three in a cross flow system at 30 °C and 30 bar. The rejection of Rose Bengal in isopropanol was conducted in repeats of three in a dead-end stirred cell (500 rpm) at 30 °C and 30 bar. The nanofiltration through a thick free standing PAR-BHPF nanofilm supported on alumina was carried out in a dead-end stirred cell (500 rpm) at 30 °C and 10 bar. The cross-flow filtration system consisted of two sets of 4 cells in series connected in parallel. The effective membrane area in each cell was 14 cm<sup>2</sup>, membrane discs were placed into 8 cross flow cells connected in series, and with a feed flow of 100 L h<sup>-1</sup>. Permeate samples for flux measurements were collected at intervals of 1 h, and samples for rejection evaluations were taken after 24 h, when steady permeate flux was achieved. Before solute rejection tests, the selected pure solvent was filtered through the membrane for 1 h in order to remove impurities, including polyethylene glycol (PEG) 400. The solute rejection test was carried out using two standard solutions. The first was a standard feed solution comprised of a homologous series of polystyrene oligomers (PS) dissolved in solvent. The solvents used were MeOH, acetone, THF, and toluene. The styrene oligomer mixture contained 2 g L<sup>-1</sup> each of PS 580 and PS 1090 (Polymer Labs, UK), and 0.01 g L<sup>-1</sup> of  $\alpha$ -methylstyrene dimer (Sigma-Aldrich, UK)<sup>50</sup>. Analysis of the styrene oligomers was undertaken using an Agilent HPLC system with UV/Vis detector set at a wavelength of 264 nm. Separation was achieved using a reverse phase column (C18-300, 250  $\times$  4.6 mm). The mobile phase consisted of 35 vol% analytical grade water and 65 vol% tetrahydrofuran with 0.1 vol% trifluoroacetic acid. The second set of standard markers solution consisted of a solution containing one of the following dyes (Sigma Aldrich) in methanol: Brilliant blue (BB, 826 g mol<sup>-1</sup>); Crystal violet (CV, 408 g mol<sup>-1</sup>); Disperse Red 1 (DR, 314 g mol<sup>-1</sup>);

and Chrysoidine G (CSG, 249 g mol<sup>-1</sup>) or Rose Bengal in isopropanol (see Supplementary Table 4). Analysis of the dyes was carried out using UV-VIS. Solvent permeance ( $J$ , L m<sup>-2</sup> h<sup>-1</sup> bar<sup>-1</sup>) was determined by measuring permeate volume ( $V$ ) per unit area ( $A$ ) per unit time ( $t$ ) per applied pressure ( $p$ ) according to the following equation:  $J=V/(A \ t \ p)$ . The rejection ( $R_i$ ) of markers was calculated from  $R_i=(1-(C_{P,i}/C_{F,i}))\times 100\%$ , where  $C_{P,i}$  and  $C_{F,i}$  correspond to marker concentrations in the permeate and the feed, respectively.

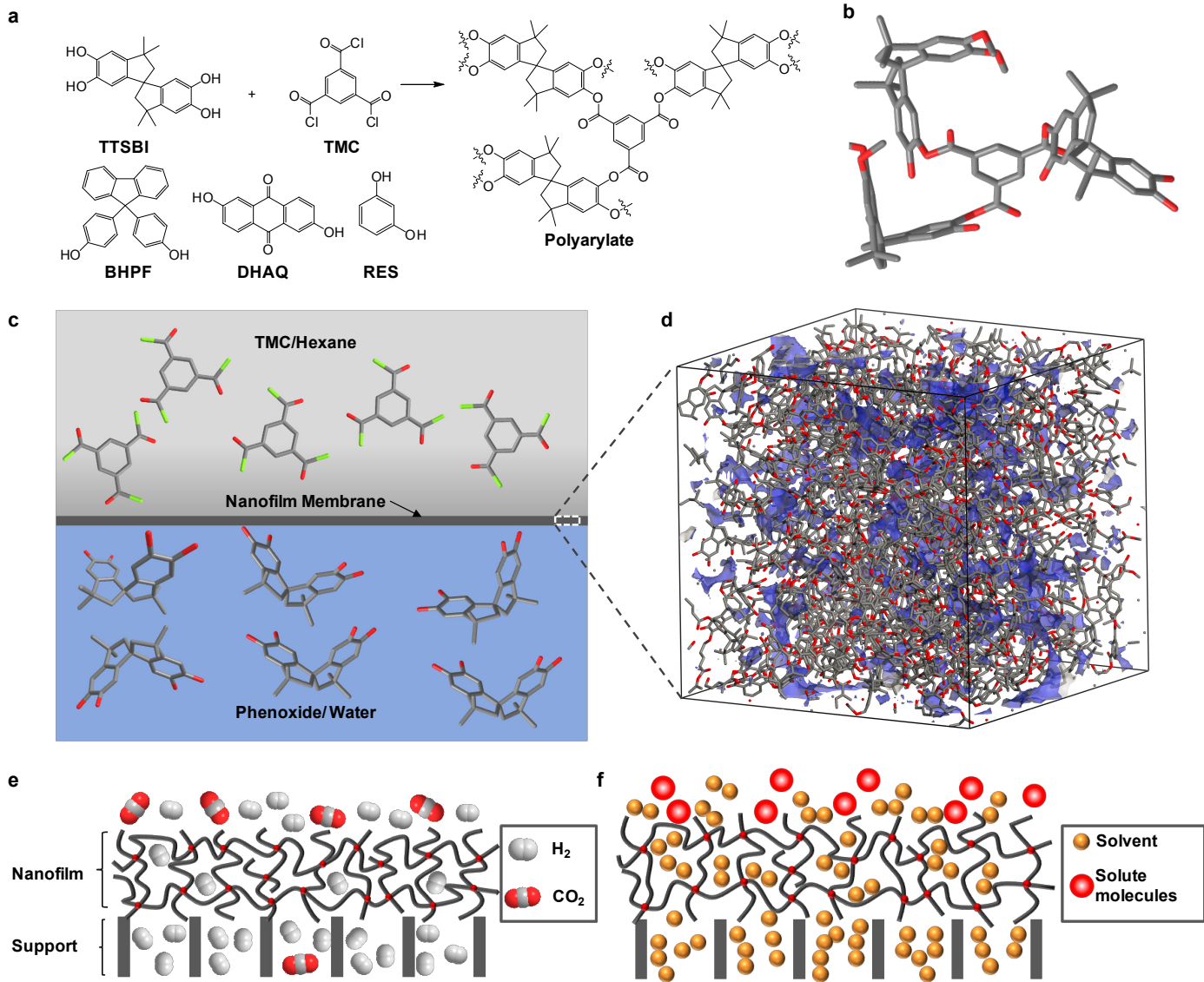
**Gas permeation.** Single gas transport properties were measured using a time-lag apparatus described in detail elsewhere<sup>9,51</sup>. The gas permeation tests were carried out at a temperature of 22 °C and feed pressure of 1 bar with He, H<sub>2</sub>, CO<sub>2</sub>, O<sub>2</sub>, N<sub>2</sub> and CH<sub>4</sub> (research grade, BOC, UK). Each membrane was thoroughly evacuated with a vacuum pump prior to measurements. The gas permeance ( $J$ , GPU, 1 GPU= 10<sup>-6</sup> cm<sup>3</sup> (STP) cm<sup>-2</sup> s<sup>-1</sup> cmHg<sup>-1</sup>) was derived from the volume of gas flowing across the membrane per unit of pressure difference. The ideal selectivity for a gas pair (A/B) is calculated from the ratio of their permeances. The uncertainties of gas permeances are within ±10 %, and selectivity within ±15 %. Intrinsic gas permeability ( $P$ ) was calculated from multiplying the permeance by the thickness of the selective polyarylate layer ( $P=J\times L$ ).  $P$  is expressed in Barrer (1 Barrer=10<sup>-10</sup> cm<sup>3</sup>(STP) cm cm<sup>-2</sup> s<sup>-1</sup> cmHg<sup>-1</sup>).

**Molecular simulation.** For the generation of amorphous polymer models, we used Polymatic<sup>47</sup>, the simulated polymerisation algorithm by Colina and coworkers<sup>52</sup>. Polymatic was originally developed for amorphous network polymers, including PIM-1<sup>52</sup>, sulfonated PIMs<sup>53</sup>, cross-linked polymers<sup>54</sup>, and CMPs<sup>55</sup>. We generated 5 models for each of the four polyarylate polymer models, PAR-BHPF, PAR-TTSBI, PAR-DHAQ, and PAR-RES. All structures were described using the polymer consistent forcefield (PCFF)<sup>56</sup>. Partial charges were calculated for the repeat units by fitting atomic charges from the output of Gaussian09<sup>57</sup> calculations at the HF/6-31G\* level of theory. The chlorides from the acyl chlorides and the hydrogens of the -OH group of the alcohols were removed in the input molecular fragments, as these are not present in the final structure. Initially we loaded periodic cubic cells, of cell dimensions of 70 Å, at low densities of 0.4 g cm<sup>-3</sup> and a ratio of 2 acyl chloride molecules to 3 phenol molecules. Polymerisation steps were then sequentially performed between reactive atoms on opposite monomers within a cutoff of 6 Å with intermediate Molecular Dynamics (MD) steps to allow the structure to adapt. The reactive end groups were the carbons of the carbonyls on the TMC and the oxygens of the alcohol molecules. The final polymerised structures were then annealed through a 21-step MD equilibration, with the protocol as detailed in the original publication of Colina *et al.*<sup>52</sup>. The LAMMPS package (<http://lammps.sandia.gov>)<sup>58</sup> was used throughout, both for the polymerisation algorithm and the 21-step relaxation procedure described by Colina *et al.*<sup>52</sup>. For any unreacted end groups after polymerisation, we terminated them appropriately, with carboxylic acid end groups for TMC and -OH end groups for the alcohol. We used carboxylic acids for the TMC as upon the polymers being exposed to water in air, all chlorides in the group would undergo hydrolysis by nucleophilic addition/elimination to form carboxylic acids. We generated 5 models for each system to ensure adequate sampling and averaged the properties across them. For void analysis, Zeo++<sup>59-60</sup> was employed. This calculates void space, the largest cavity diameter, pore limiting diameter, pore size distribution and through a Voronoi decomposition the interconnectivity of void space. The surface area accessible to N<sub>2</sub> was calculated with a probe radius of 1.55 Å, equivalent to the van der Waals radius of N<sub>2</sub>. The atomic radii for the host and for N<sub>2</sub> were taken from the Cambridge Crystallographic Database Centre (CCDC) guidelines (<http://www.ccdc.cam.ac.uk/products/csd/radii>).

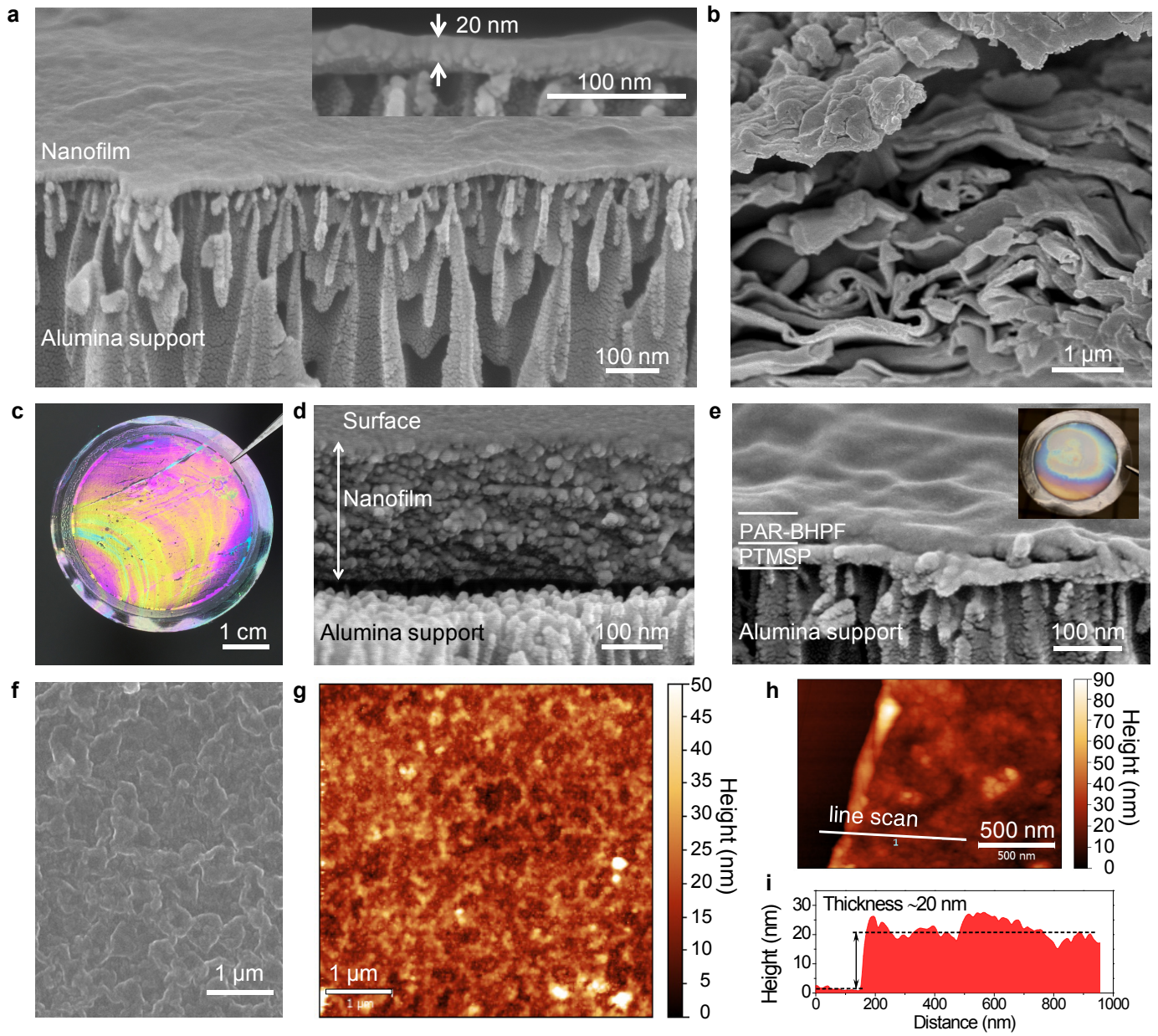
## References

48. See Toh, Y. H., Lim, F. W., & Livingston, A. G., Polymeric membranes for nanofiltration in polar aprotic solvents. *J. Membr. Sci.* **301**, 3-10 (2007).
49. Stafford, C. M. *et al.*, A buckling-based metrology for measuring the elastic moduli of polymeric thin films. *Nat. Mater.* **3**, 545-550 (2004).
50. See Toh, Y. H. *et al.*, In search of a standard method for the characterisation of organic solvent nanofiltration membranes. *J. Membr. Sci.* **291**, 120-125 (2007).
51. Song, Q. *et al.*, Zeolitic imidazolate framework (ZIF-8) based polymer nanocomposite membranes for gas separation. *Energy Environ. Sci.* **5**, 8359-8369 (2012).
52. Abbott, L., Hart, K., & Colina, C., Polymatic: A generalized simulated polymerization algorithm for amorphous polymers. *Theoretical Chemistry Accounts C7 - 1334* **132**, 1-19 (2013).
53. Hart, K. E., Abbott, L. J., McKeown, N. B., & Colina, C. M., Toward effective CO<sub>2</sub>/CH<sub>4</sub> separations by sulfur-containing pims via predictive molecular simulations. *Macromolecules* **46**, 5371-5380 (2013).
54. Abbott, L. J., Hughes, J. E., & Colina, C. M., Virtual synthesis of thermally cross-linked copolymers from a novel implementation of polymatic. *The Journal of Physical Chemistry B* **118**, 1916-1924 (2014).

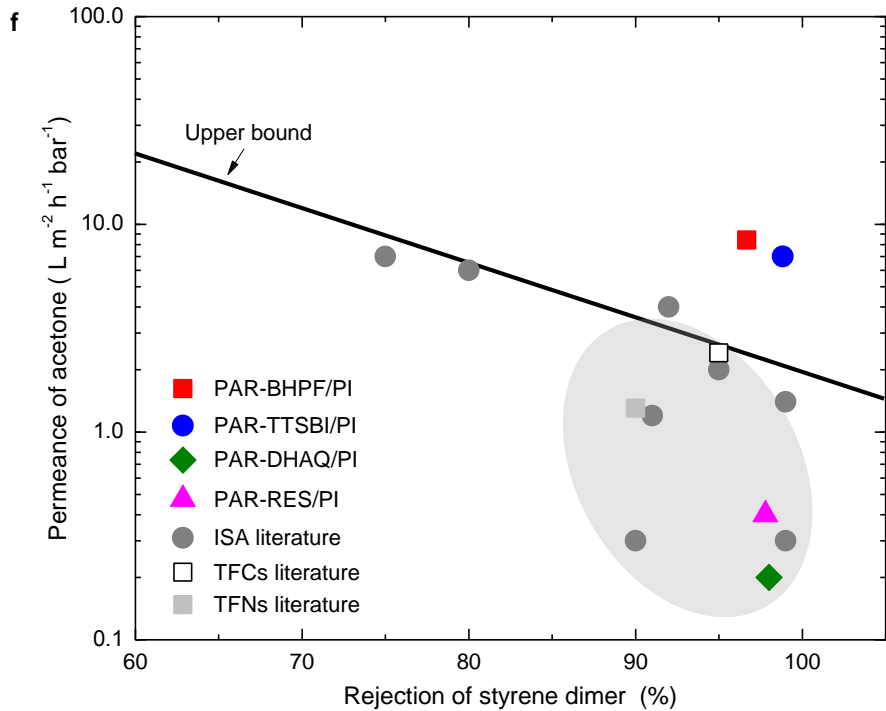
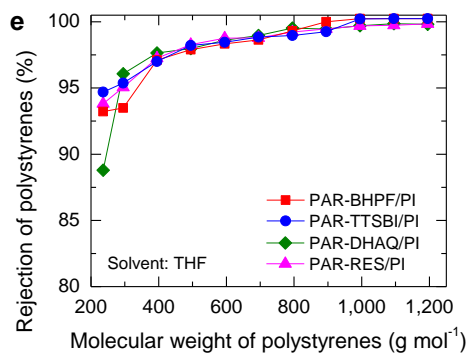
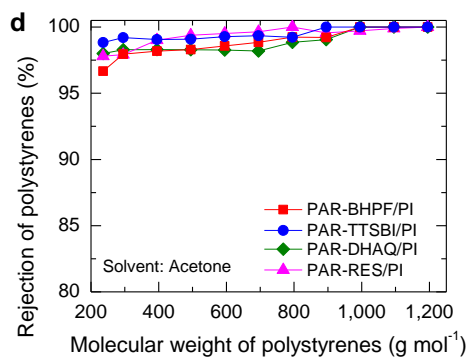
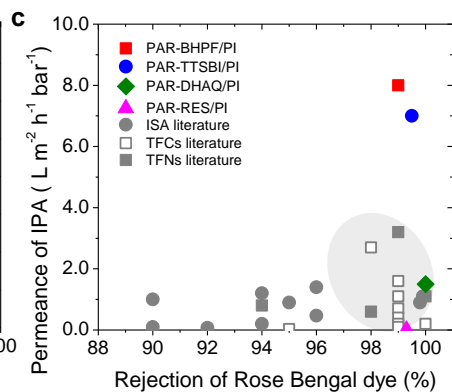
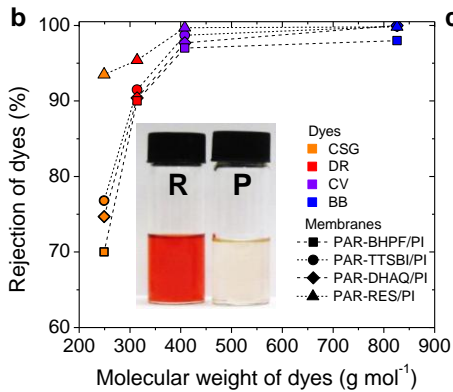
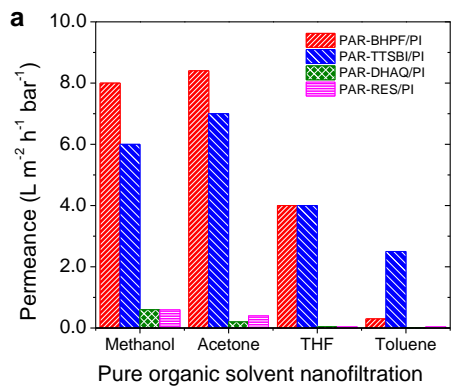
55. Abbott, L. J. & Colina, C. M., Porosity and ring formation in conjugated microporous polymers. *Journal of Chemical & Engineering Data* **59**, 3177-3182 (2014).
56. Sun, H., Force field for computation of conformational energies, structures, and vibrational frequencies of aromatic polyesters. *J. Comput. Chem.* **15**, 752-768 (1994).
57. Frisch, M. J. *et al.*, Gaussian 09. Revision A.02, Gaussian, Inc., Wallingford CT, USA. (2009).
58. Plimpton, S., Fast parallel algorithms for short-range molecular dynamics. *J. Comput. Phys.* **117**, 1-19 (1995).
59. Willems, T. F. *et al.*, Algorithms and tools for high-throughput geometry-based analysis of crystalline porous materials. *Microporous Mesoporous Mater.* **149**, 134-141 (2012).
60. Pinheiro, M., Martin, R. L., Rycroft, C. H., & Haranczyk, M., High accuracy geometric analysis of crystalline porous materials. *CrystEngComm* **15**, 7531-7538 (2013).

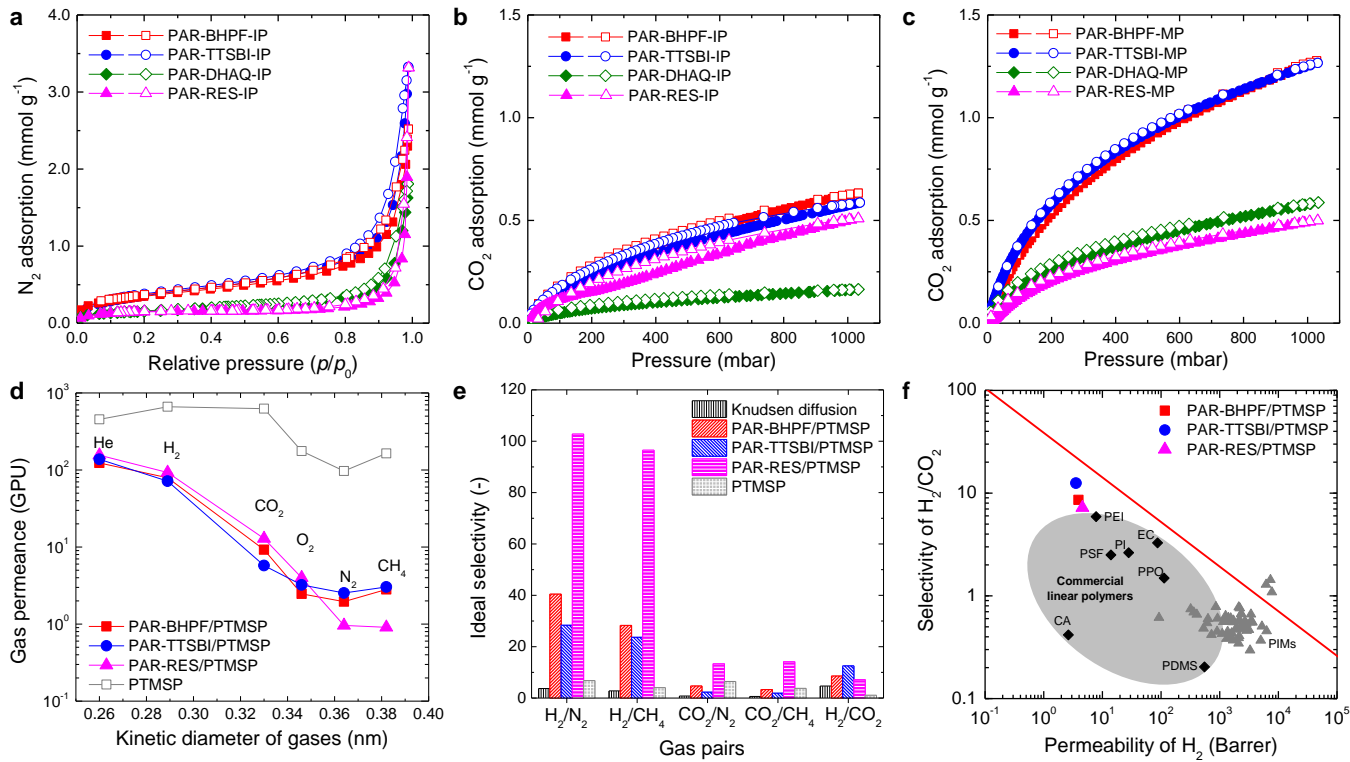


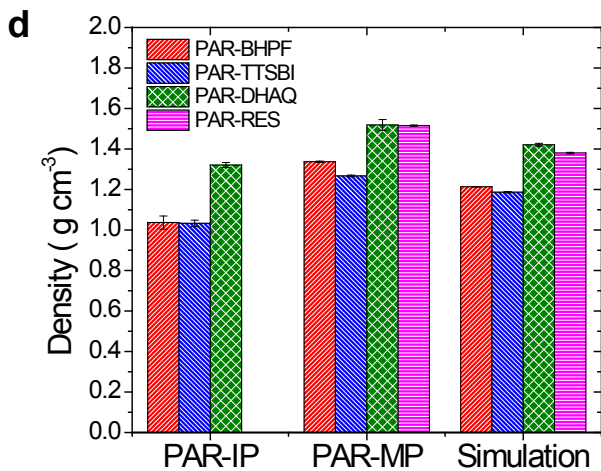
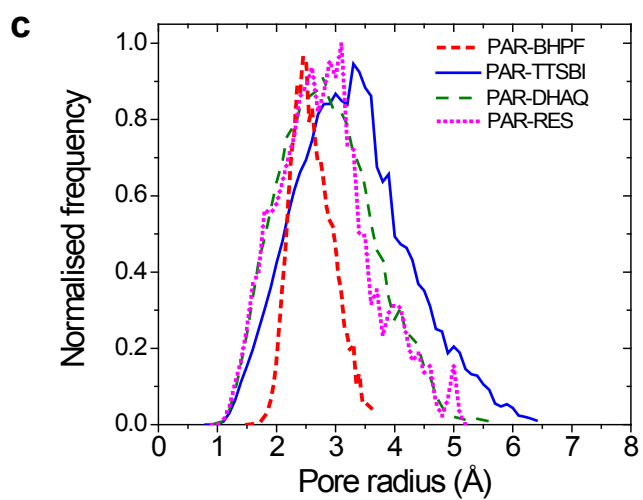
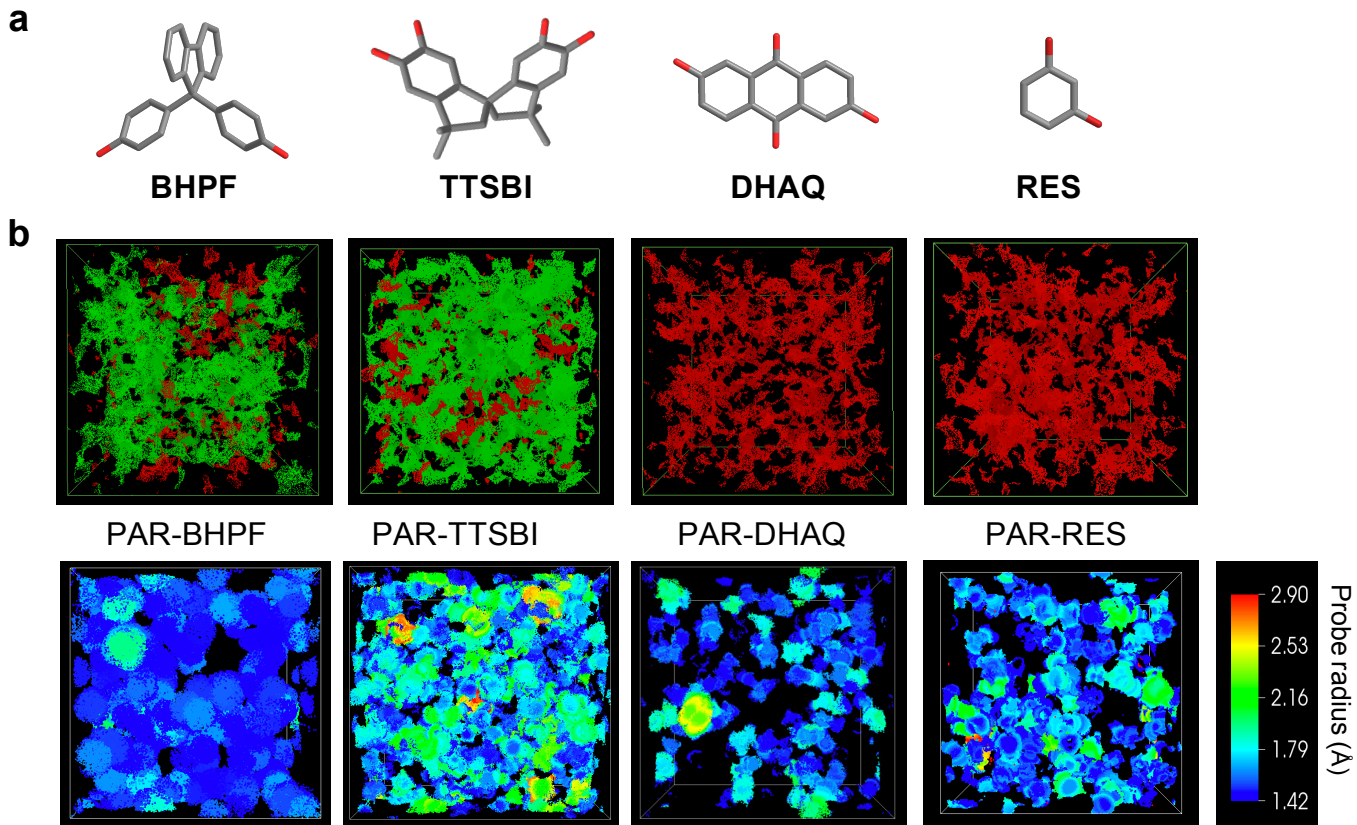












# Polymer nanofilms with enhanced microporosity by interfacial polymerisation

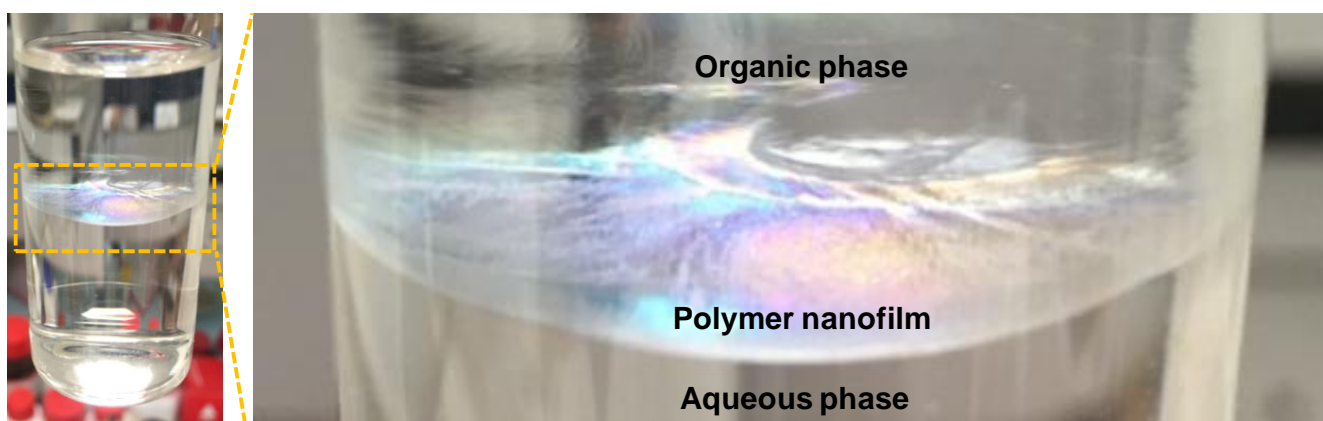
Maria F. Jimenez-Solomon<sup>1†</sup>, Qilei Song<sup>1†</sup>, Kim E. Jelfs<sup>2</sup>, Marta Munoz-Ibanez<sup>1</sup> and Andrew G. Livingston<sup>1\*</sup>

<sup>1</sup>Department of Chemical Engineering, Imperial College London, London SW7 2AZ, UK,

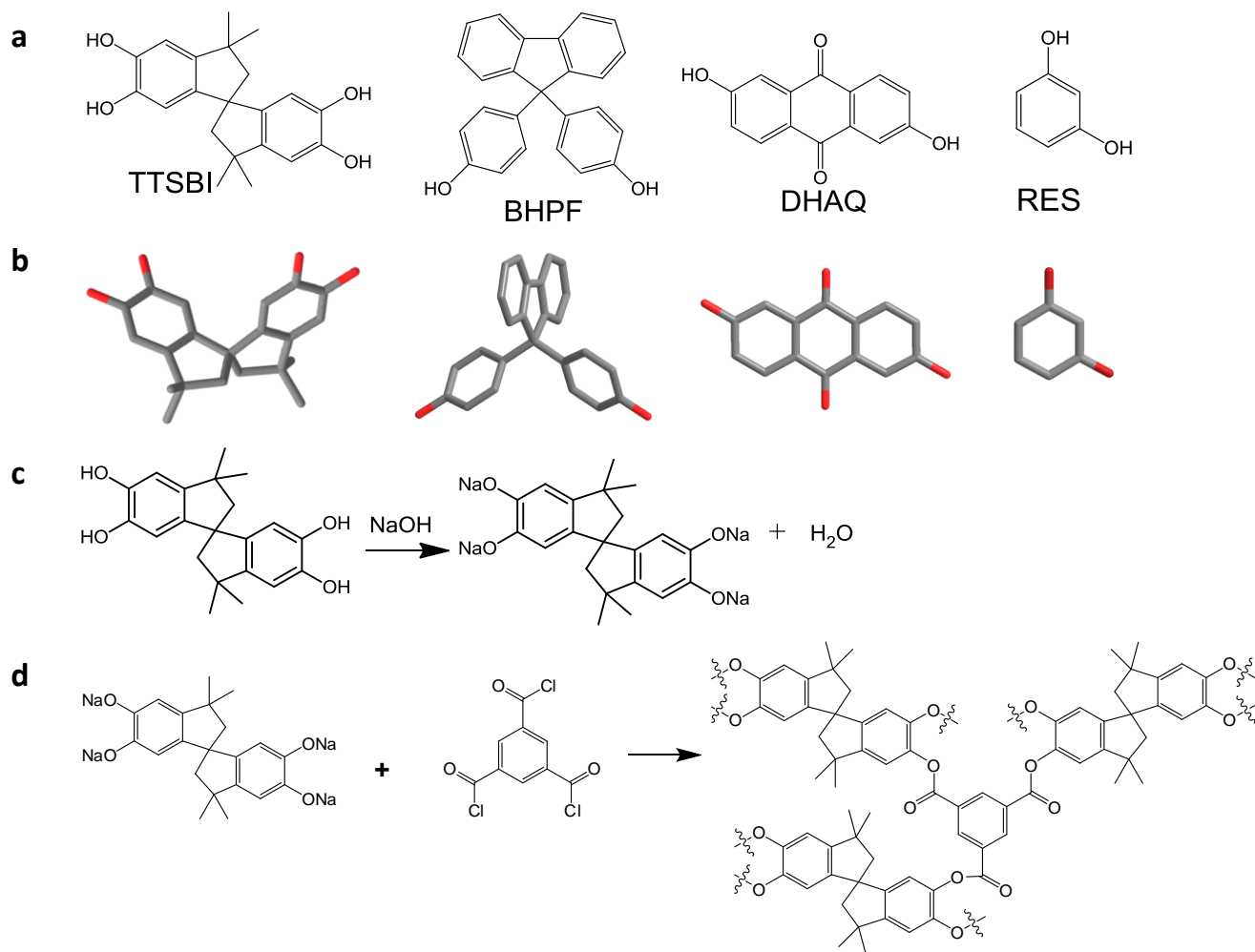
<sup>2</sup>Department of Chemistry, Imperial College London. London SW7 2AZ, UK.

<sup>†</sup>These authors contributed equally to this work.

\* e-mail: [a.livingston@imperial.ac.uk](mailto:a.livingston@imperial.ac.uk)

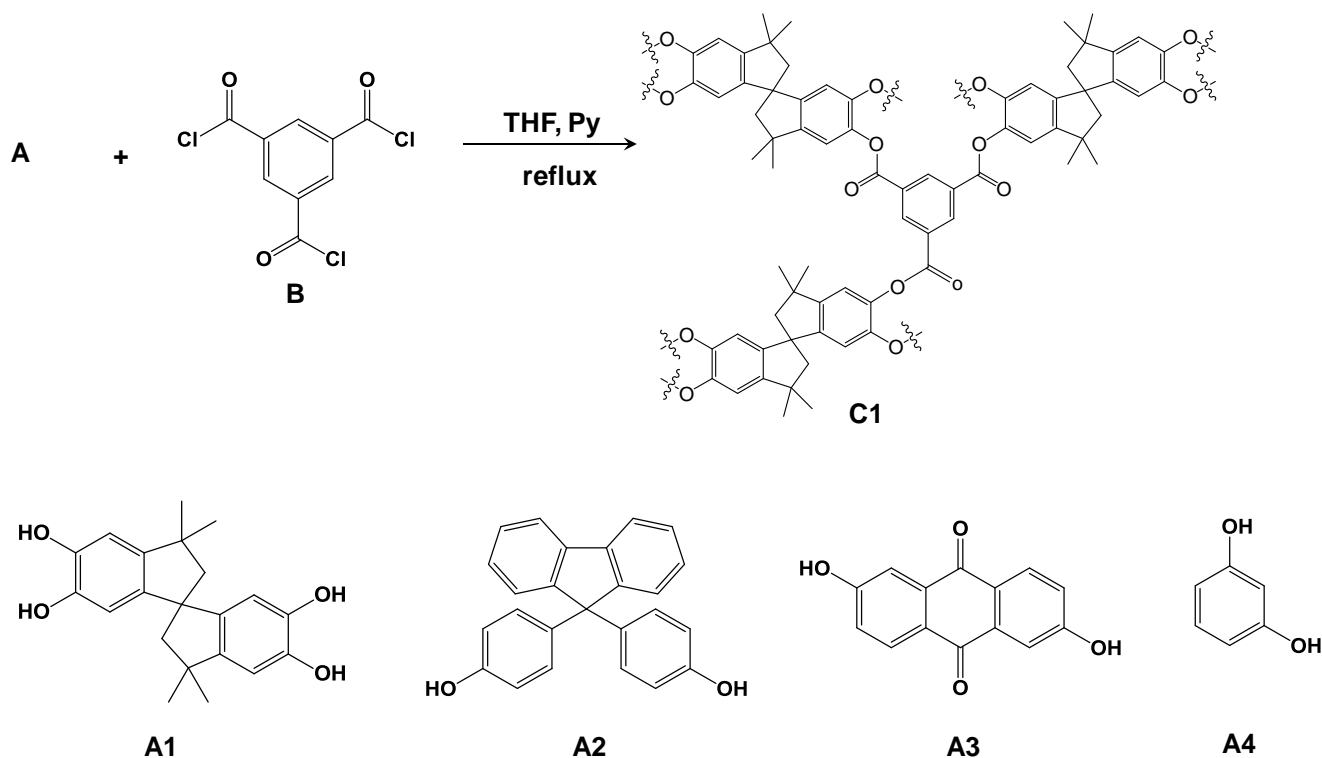


**Supplementary Figure 1. Synthesis of an ultrathin free-standing PAR nanofilm by interfacial polymerisation.** A photograph of a glass vial containing two immiscible solutions: TMC (0.1 wt%) in hexane (top) and BHPF (1 wt%) in NaOH/water (bottom). A polyarylate nanofilm is formed between the two phases by interfacial polymerisation.

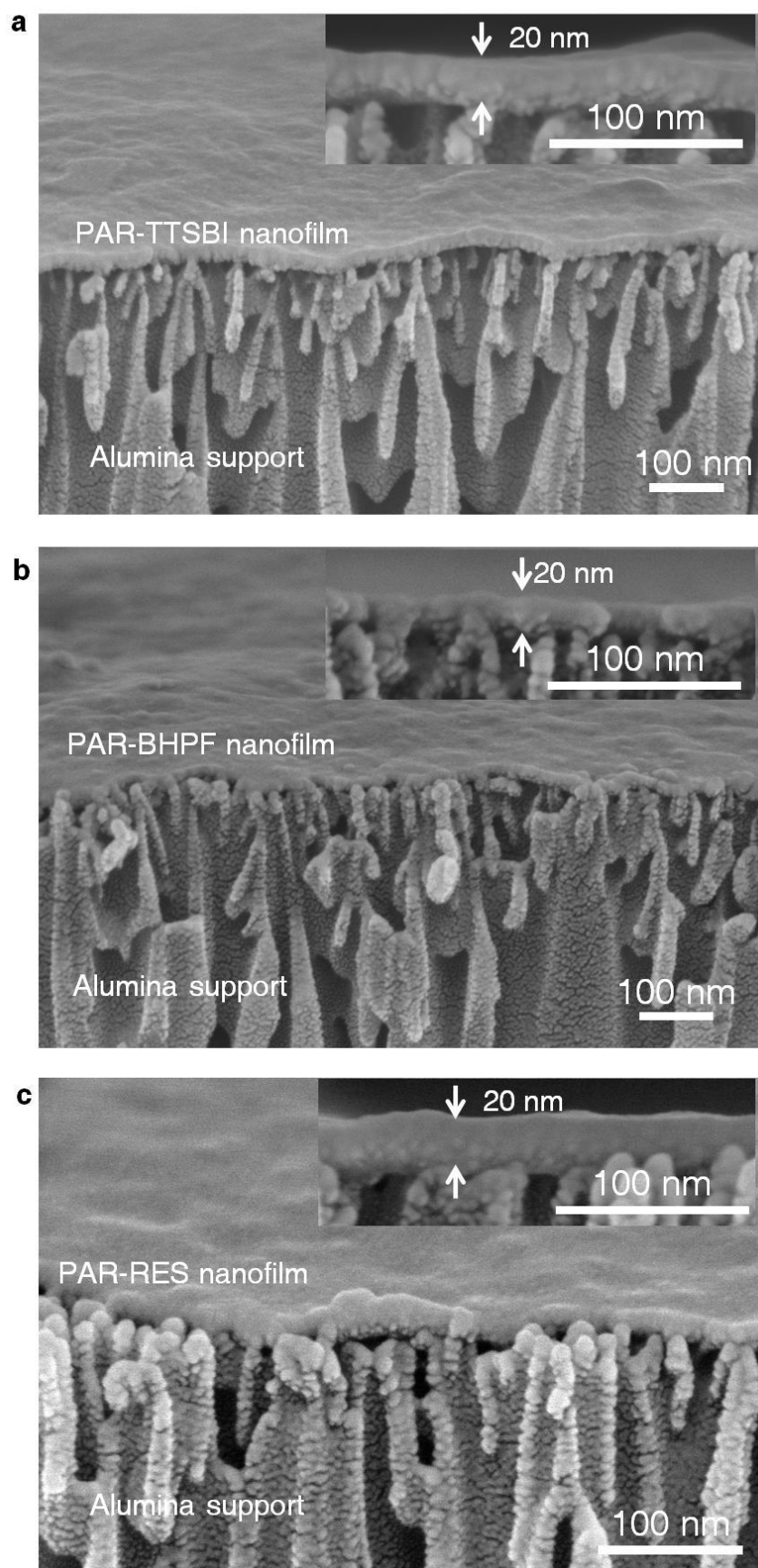


**Supplementary Figure 2. Synthesis of polyarylate (PAR) network polymers by interfacial polymerisation.**

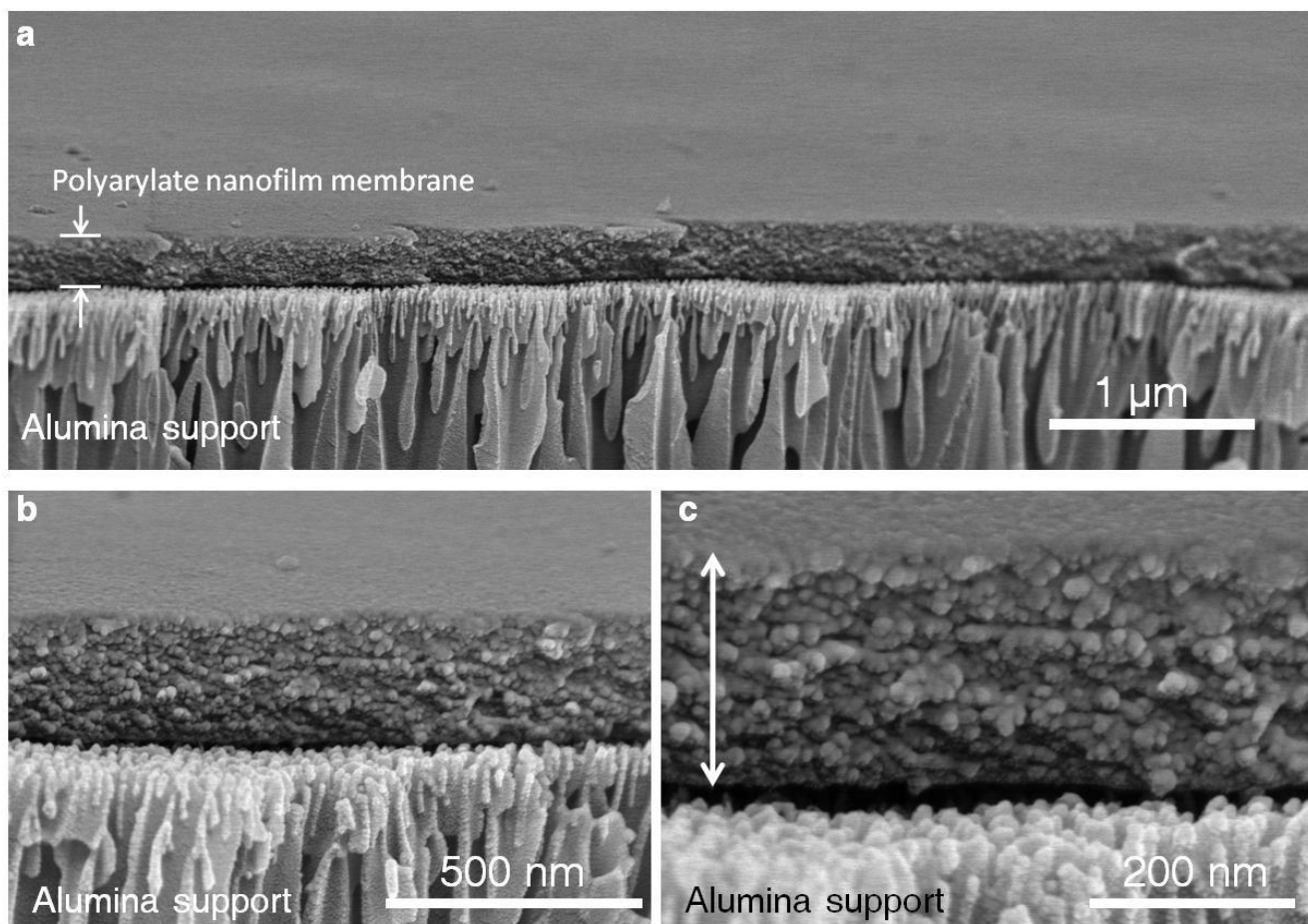
**a**, Four different phenol monomers were used to form four crosslinked polyarylate materials: including contorted monomers: 5,5',6,6'-tetrahydroxy-3,3,3',3'-tetramethylspirobisindane (TTSBI); 9,9-Bis(4-hydroxyphenyl)fluorene (BHPF); planar monomers: 2,6-Dihydroxyanthraquinone (DHAQ); 1,3-benzenediol, resorcinol monomer (RES); **b**, Molecular model of four phenol monomers used. Each phenol was dissolved in a dilute sodium hydroxide aqueous solution (pH=13) and reacted interfacially with trimesoyl chloride dissolved in hexane; **c**, formation of TTSBI phenoxide when phenol is dissolved in diluted NaOH aqueous solution; **d**, shows the reaction of TTSBI phenoxide with trimesoyl chloride to form a spiro-structured PAR-TTSBI network.



**Supplementary Figure 3. Synthesis of polyarylate network polymers by monophasic reaction.** **A1:** 5,5',6,6'-tetrahydroxy-3,3,3',3'-tetramethylspirobisindane (TTSBI); **A2:** 9,9-Bis(4-hydroxyphenyl)fluorene (BHPF); **A3:** 2,6-Dihydroxyanthraquinone (DHAQ); **A4:** 1,3-benzenediol (RES), **B:** trimesoyl chloride (TMC); THF: tetrahydrofuran; Py: pyridine; C1(Spiro): TTSBI polyarylate network. Polyarylate solids were prepared by monophasic reactions following a synthesis method published elsewhere<sup>1</sup>. 1 g phenol was mixed with TMC at 1:1 molar ratio dissolved in dry degassed THF (40-60 mL). An 11-fold molar excess of dry pyridine was added through a syringe under nitrogen gas and stirring. After reflux for 20 h, a precipitate was formed, which was washed with 1M HCl solution, water and THF. It was subsequently dried via freeze drying, and then at 120 °C in a vacuum oven for 12h. Detailed reaction conditions: TTSBI (1 g) with TMC (0.78 g), in 40 mL of THF and 2.6 mL of pyridine; BHPF (1 g) with TMC (0.78 g) in 40 mL of THF and 2.6 mL of pyridine; DHAQ (1 g) with TMC (1.04 g) in 40 mL of THF and 3.5 mL of pyridine; and RES (1 g) with TMC (2.41 g) in 60 mL of THF and 8 mL of pyridine.

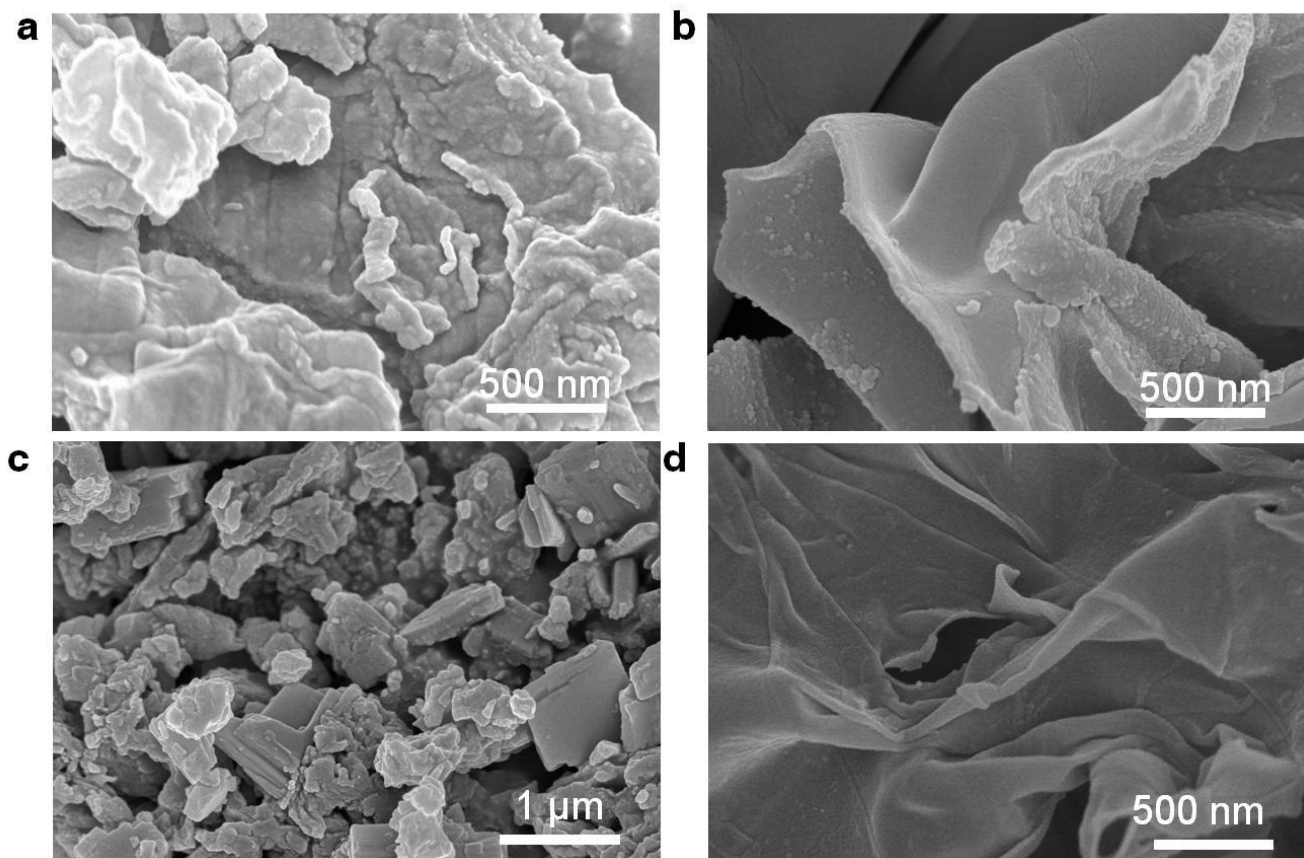


**Supplementary Figure 4. Cross-sectional SEM images of ultra-thin interfacially polymerised polyarylate nanofilms supported on alumina. a, PAR-TTSBI; b, PAR-BHPF; c, PAR-RES.** The nanofilms were prepared by interfacial polymerisation of TMC (0.1 wt%) in hexane with TTSBI(1 wt%), or BHPF (1 wt%) or RES (2 wt%) in NaOH/water. The samples were formed at the interface and transferred onto alumina supports.

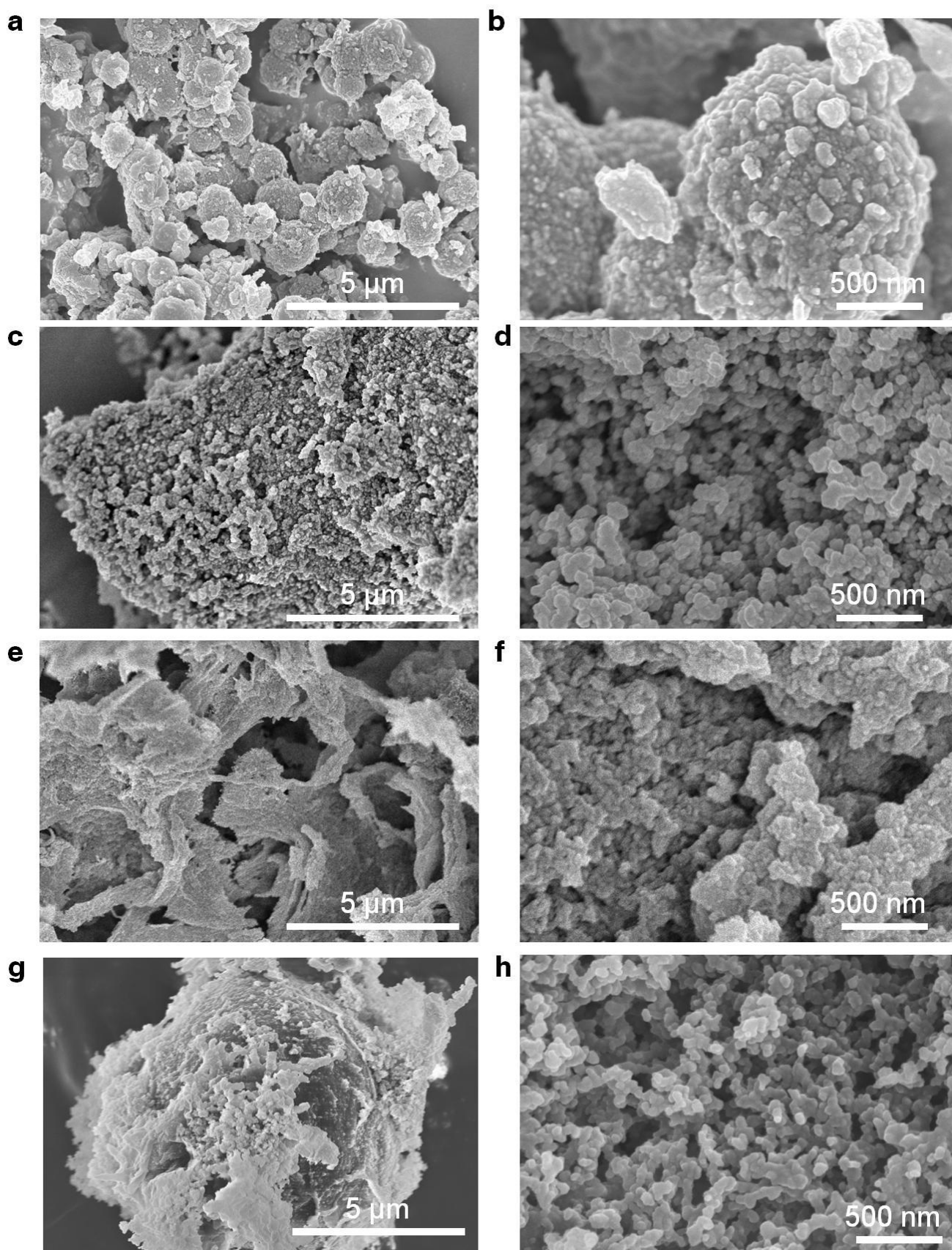


**Supplementary Figure 5. Cross-sectional SEM images of free-standing defect-free polyarylate nanofilms (200 nm) supported on porous alumina discs at various magnifications.** The nanofilm was prepared by interfacial polymerisation of TMC (1 wt%) in hexane with BHPF (1 wt%) in NaOH/water at the interface and transferred onto alumina supports.

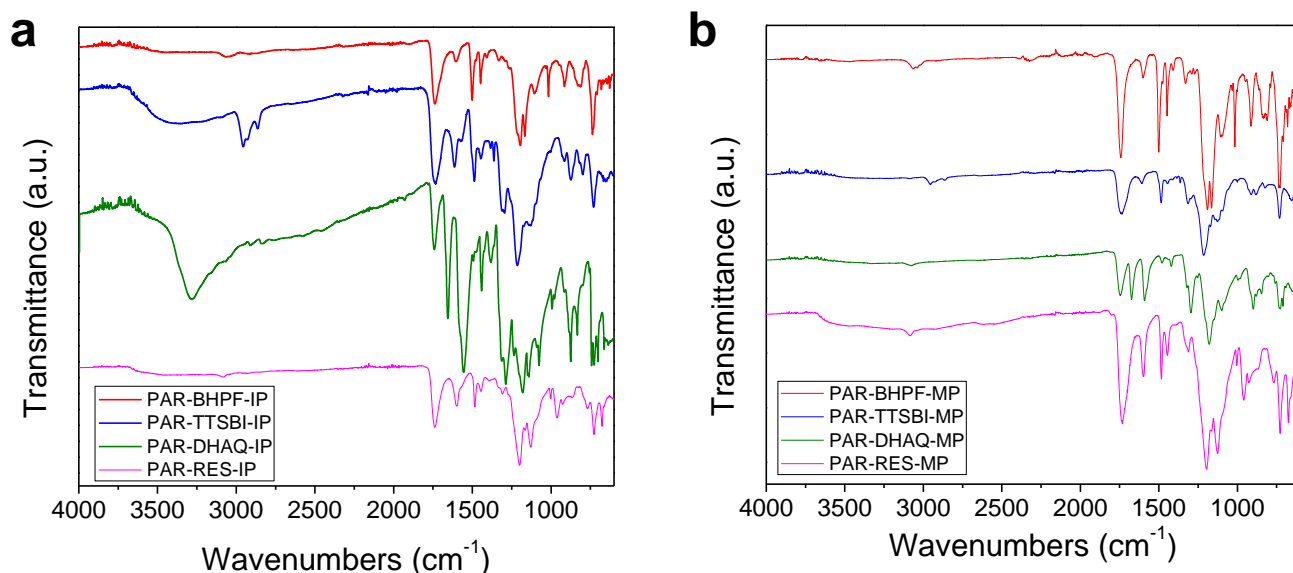




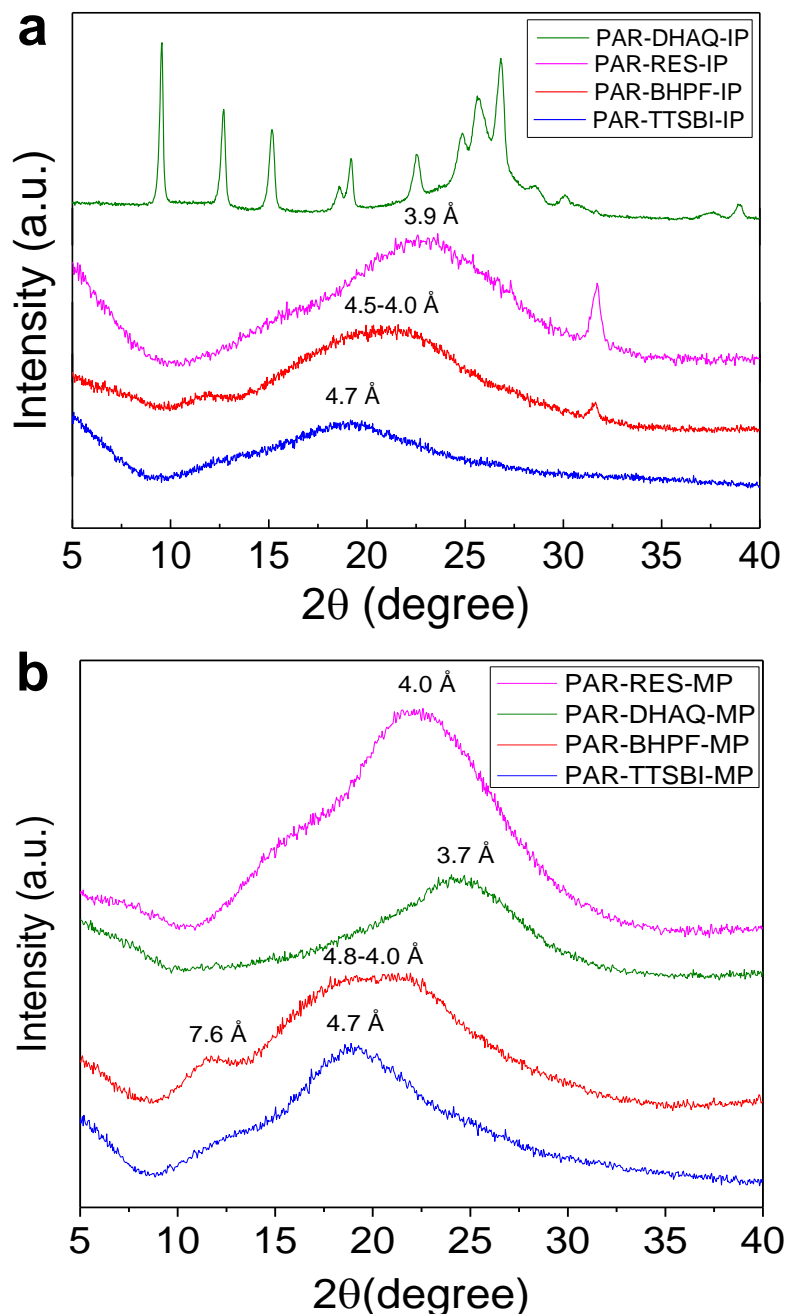
**Supplementary Figure 6. SEM images of polyarylate powders made by interfacial polymerisation.** The samples were synthesised via interfacial polymerisation through rigorous mixing of a solution of TMC in hexane added to a solution of each phenol in NaOH/water. **a**, spiro-structured polyarylate (PAR-TTSBI) with stacked films observed; **b**, Cardo-structured polyarylate (PAR-BHPF) with cross-sections observed; **c**, planar-structured PAR-DHAQ (crystal-like morphology was observed which may be due to the crystallization of residual monomers trapped in the network); **d**, planar-structured PAR-RES with cross-sections observed. Four different phenol monomers were used to form each polyarylate network (Supplementary Fig. 2). Each phenol monomer was dissolved in a diluted sodium hydroxide aqueous solution (pH=13) with a molar ratio of 4:1 (NaOH to TTSBI and BHPF), and 2:1 (NaOH to DHAQ and RES) (throughout this study), with concentrations of TTSBI (1 wt%), BHPF (1 wt%), DHAQ (2 wt%), and RES (2 wt%). The sodium phenoxides were then reacted interfacially with TMC dissolved in hexane (0.2 wt % by volume) under rigorous stirring for 2 min. The resulting polymers were then washed thoroughly with water, followed by hexane. They were then freeze dried from hexane and dried at 120 °C in a vacuum oven for 12h.



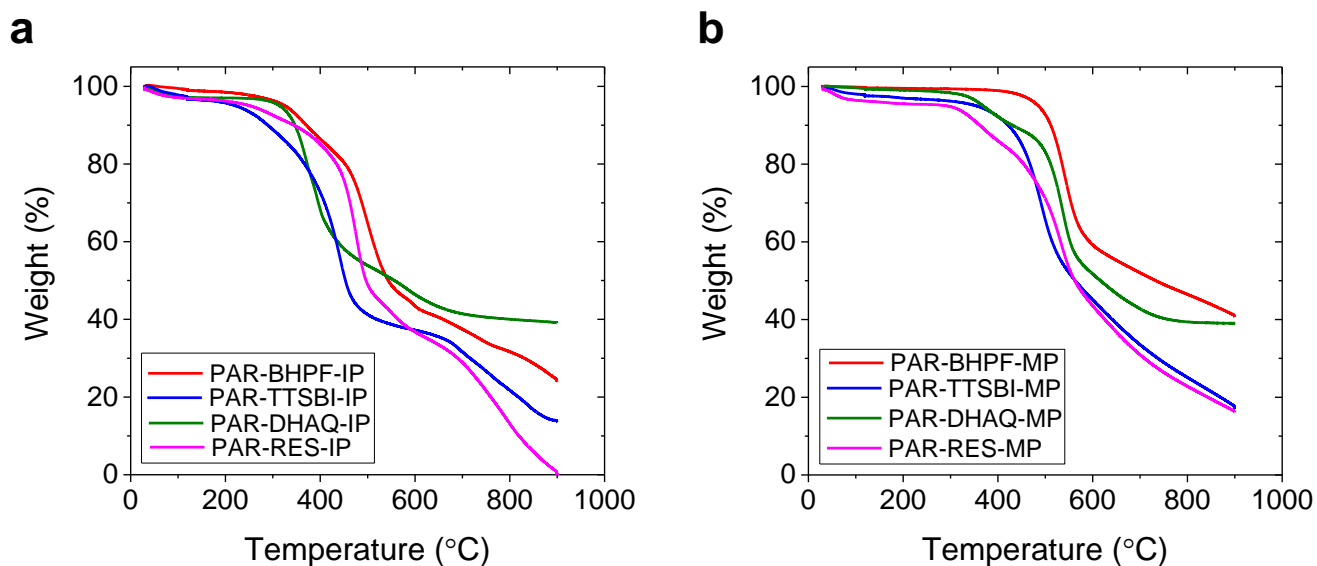
**Supplementary Figure 7. SEM images of surfaces of polyarylate network powders synthesised by monophasic reactions.** The samples were synthesised via monophasic (MP) reaction of TMC and phenol dissolved in THF under reflux catalysed by pyridine. (a-b), PAR-TTSBI; (c-d), PAR-BHPF; (e-f), PAR-DHAQ; (g-h), PAR-RES.



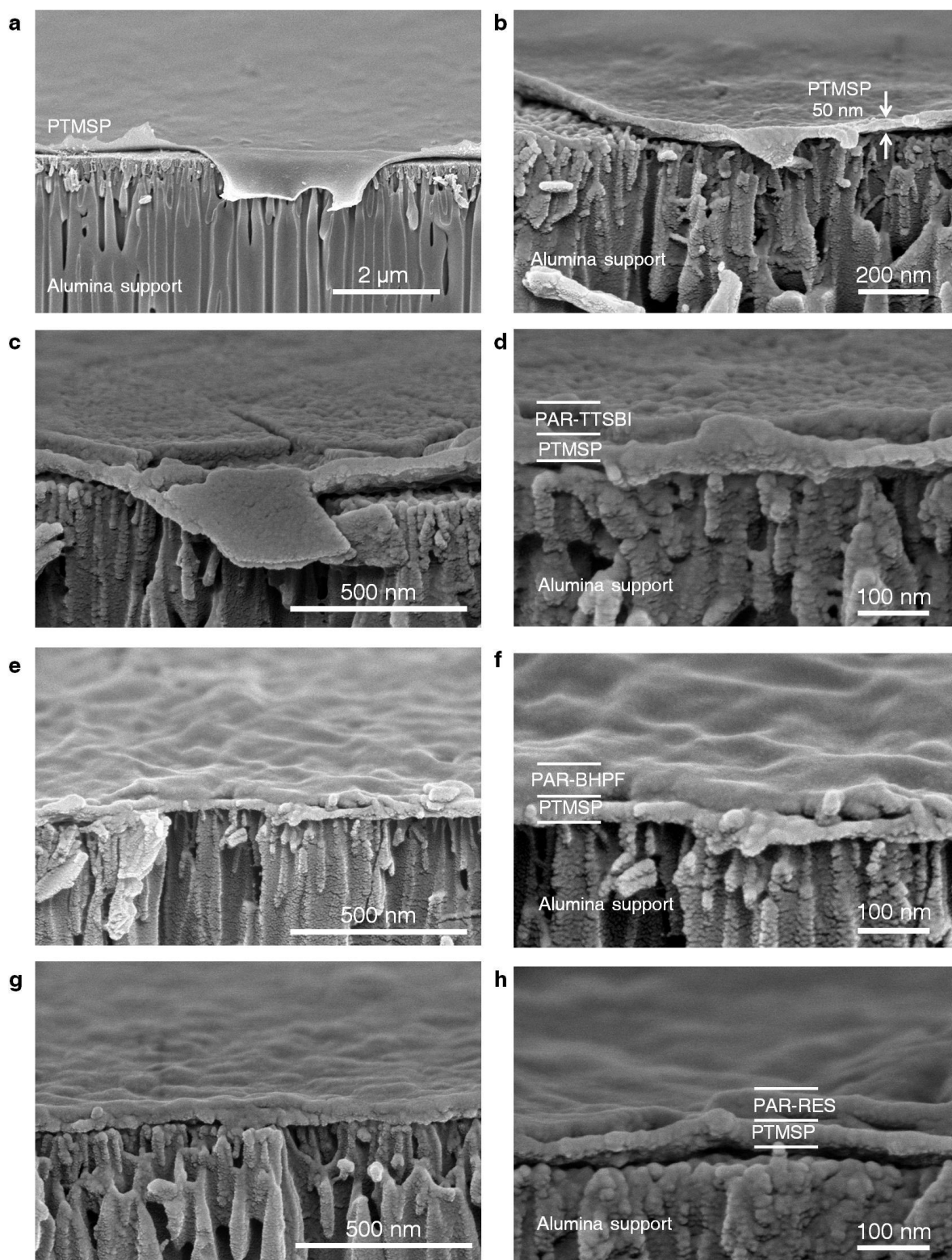
**Supplementary Figure 8. Fourier-transform infrared (FTIR) spectra.** **a**, FT-IR spectra of polymer powders synthesized via interfacial polymerisation (IP) with rigorous stirring; **b**, FT-IR spectra of polymer powders synthesized via monophasic (MP) reaction. The FT-IR spectra show the carbonyl group (C=O) stretching at about 1750-1735  $\text{cm}^{-1}$ , which corresponds to the C=O stretching in the ester groups. C-O stretching (1250-1150  $\text{cm}^{-1}$ ). PAR-DHAQ-IP shows a peak at around 3250  $\text{cm}^{-1}$  corresponding to residual DHAQ monomer entrapped in the polymer network.



**Supplementary Figure 9. Wide-angle X-ray scattering patterns of polyarylate polymers. a,** Polyarylate powders synthesised by interfacial polymerisation (IP) of immiscible solutions of TMC/hexane and phenoxide/water with rigorous stirring. **b,** polyarylates powders synthesised by monophasic (MP) reaction. Note that PAR- DHAQ polymer prepared by interfacial polymerisation shows crystalline peaks which may be due to the crystallization of residual monomers trapped in the network. Monophasic synthesis of the PAR-DHAQ polymer confirms that it is essentially amorphous.

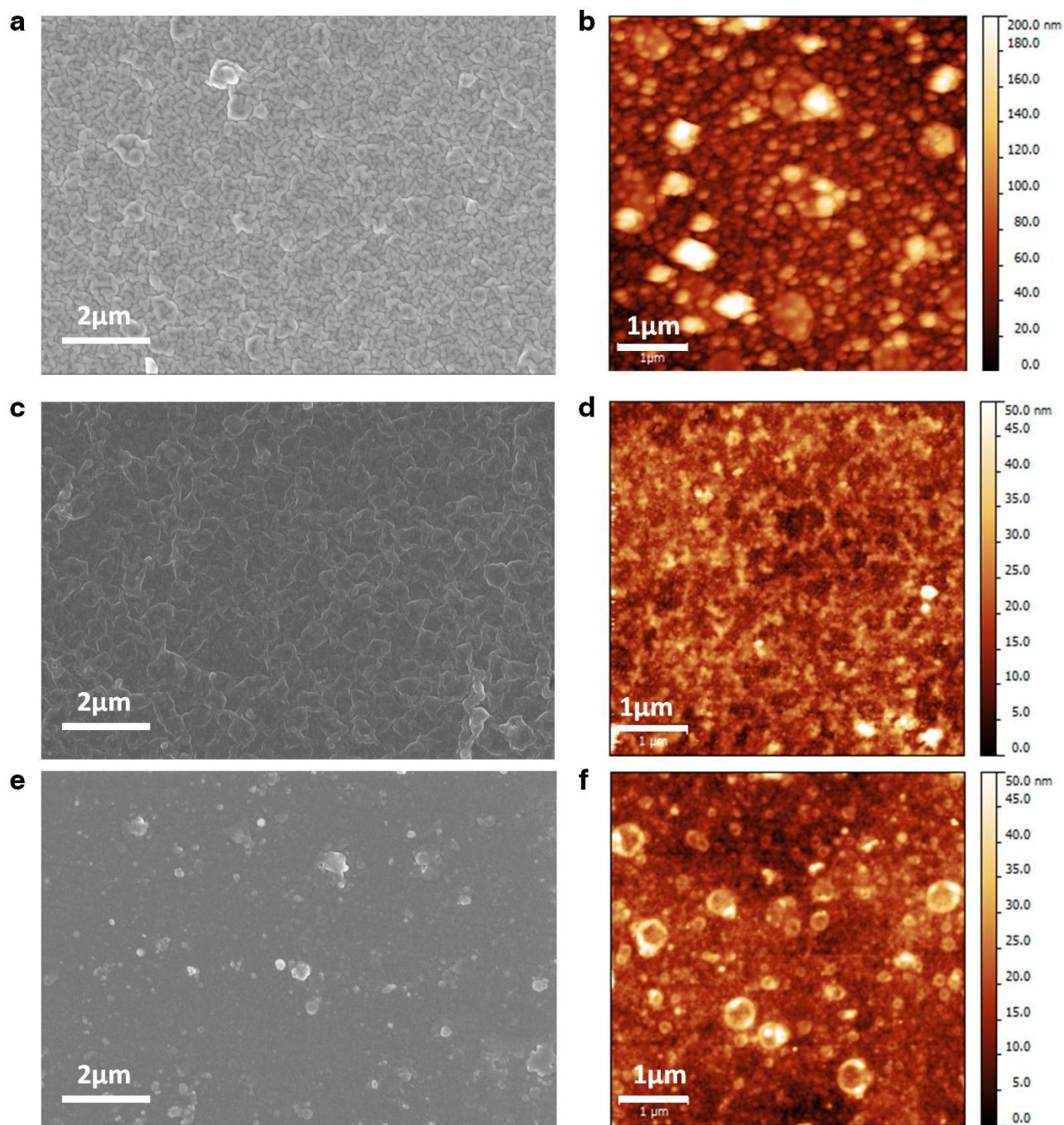


**Supplementary Figure 10. Thermogravimetric analysis (TGA) curves of polyarylate powders. a,** TGA curves of polymer powders synthesized via interfacial polymerisation (IP) obtained by rigorous mixing of a solution of TMC in hexane added to a solution of each phenol in NaOH/water; **b,** TGA curves of polymer powders synthesized via monophasic (MP) reaction of TMC and phenol dissolved in THF under reflux in pyridine.

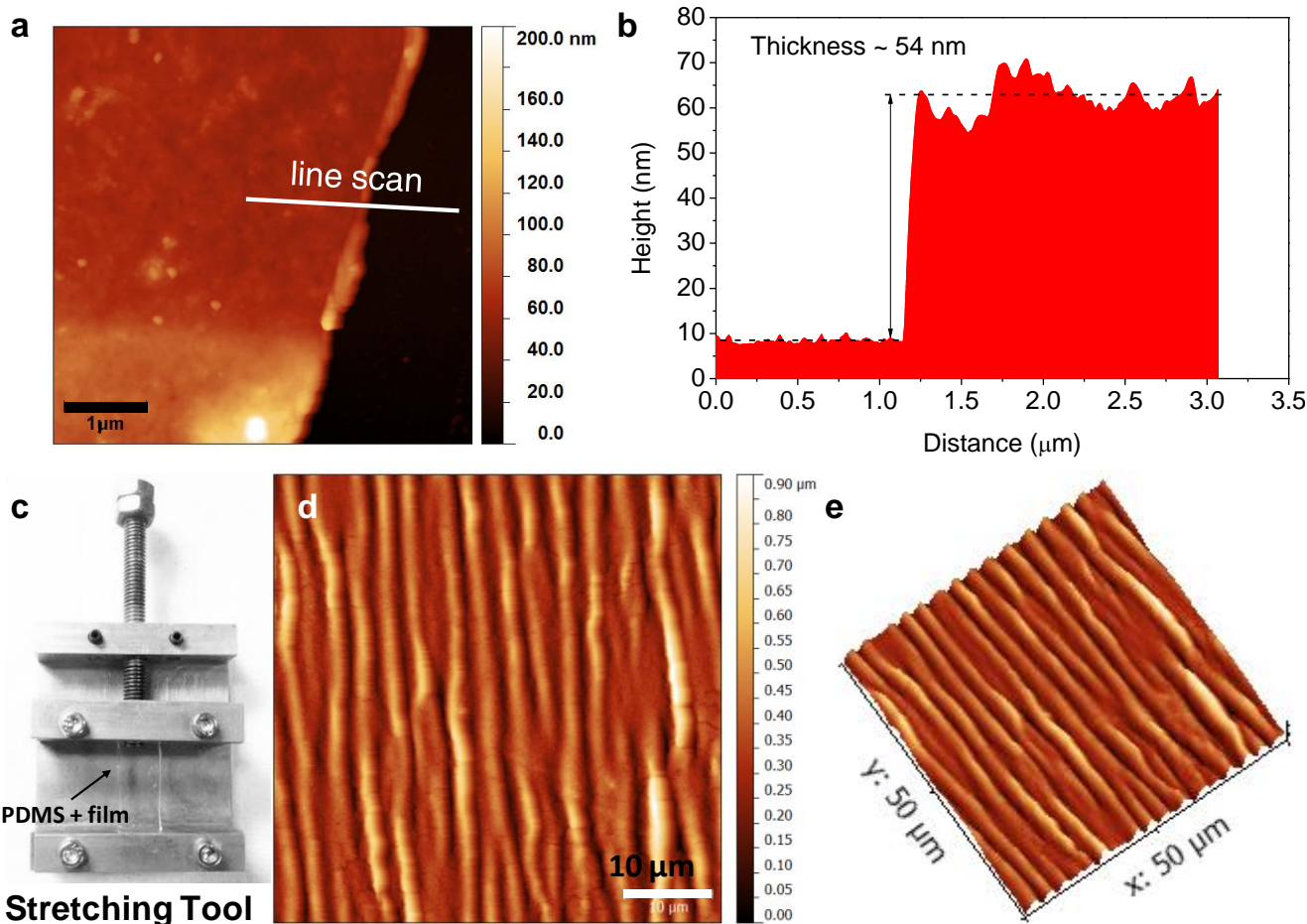


**Supplementary Figure 11. Cross-sectional SEM images of interfacially polymerised polyarylate nanofilms.** (a-b), a thin layer of PTMSP polymer coated on porous anodised aluminium oxide discs. (c-d) PAR-TTSBI, (e-f) PAR-BHPF, and (g-h) PAR-RES nanofilms made on PTMSP/alumina membranes. A thin layer of PTMSP polymer (50 nm) was coated on the alumina support first as an intermediate layer, then PAR nanofilms were prepared by sequential spin-coating of a solution of TMC in hexane (1 wt%), and a solution of phenol in NaOH/water (1 wt%). The average thicknesses of PAR nanofilms are approximately the same (~ 50 nm).



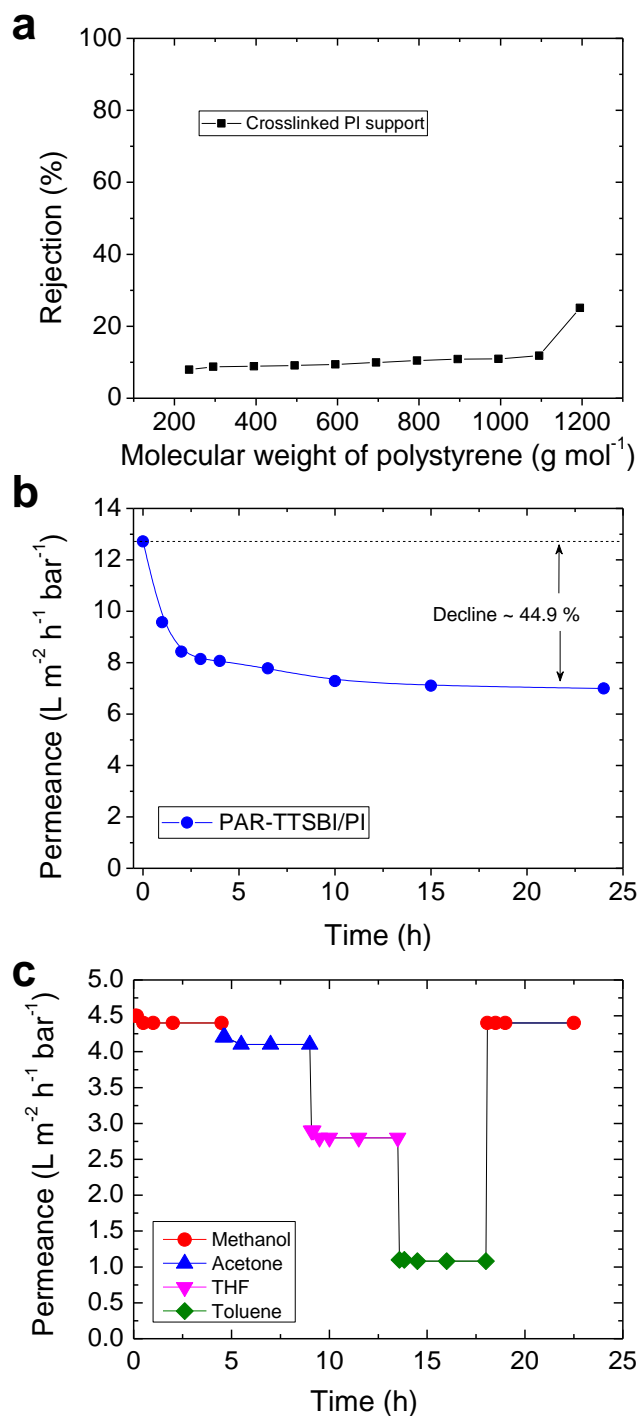


**Supplementary Figure 12. SEM and AFM images of interfacially polymerised polyarylate nanofilms on crosslinked polyimide P84 support membrane (PAR/PI). a**, SEM image of surface of PAR-RES/PI nanofilm composite membrane. **b**, AFM image probed on the sample shown in (a). **c**, SEM image of surface of PAR-TTSBI/PI nanofilm composite membrane. **d**, AFM image probed on the sample shown in (c). **e**, SEM image of surface of PAR-DHAQ/PI nanofilm composite membrane. **f**, AFM image probed on the sample shown in (e).

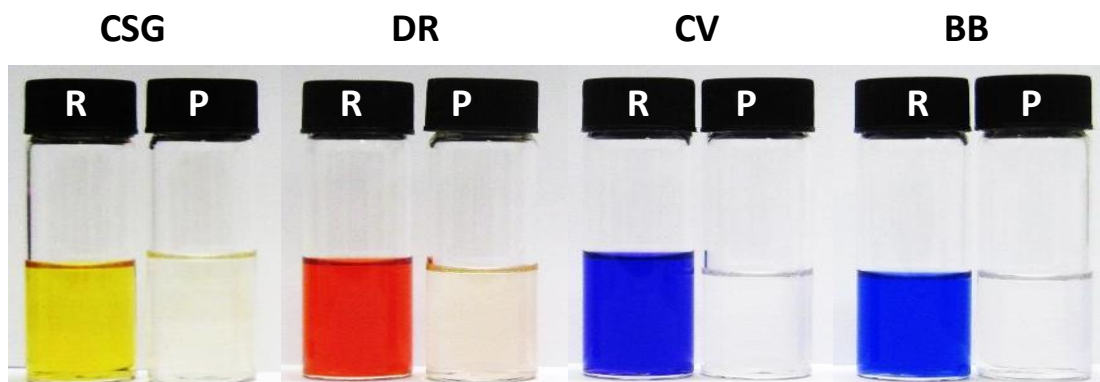


**Supplementary Figure 13. Mechanical properties of spiro-structured PAR-TTSBI freestanding nanofilm.** **a**, AFM image of the free-standing spiro-structured PAR-TTSBI nanofilm. **b**, Height profile along the line indicated in (a). **c**, Photograph of the stretching tool. Poly(dimethylsiloxane) (PDMS) strips (20 mm × 15 mm) with a thickness of 1.55 mm were stretched 10 % using the stretching tool. The free standing PAR-TTSBI nanofilm was transferred on to stretched PDMS following a procedure similar to that previously described<sup>2-3</sup>. After peeling off the polypropylene nonwoven, a membrane coupon was pressed with the polyarylate side facing down, onto a stretched PDMS strip by placing a drop of ethanol at the interface, and then dried in air. The polyimide support was then completely removed by dissolving through adding DMF drops, followed by rinsing with isopropanol, and left to dry. The PDMS was then unstretched, generating compressive stress in the nanofilm, resulting in aligned wrinkles normal to the elongation direction. Wrinkle patterns were observed under AFM for the PAR-TTSBI nanofilm. **d**, and **e**, AFM images of the wrinkles formed when the PAR-TTSBI free standing nanofilm is transferred onto an elastomer substrate and subjected to an applied compressive stress.

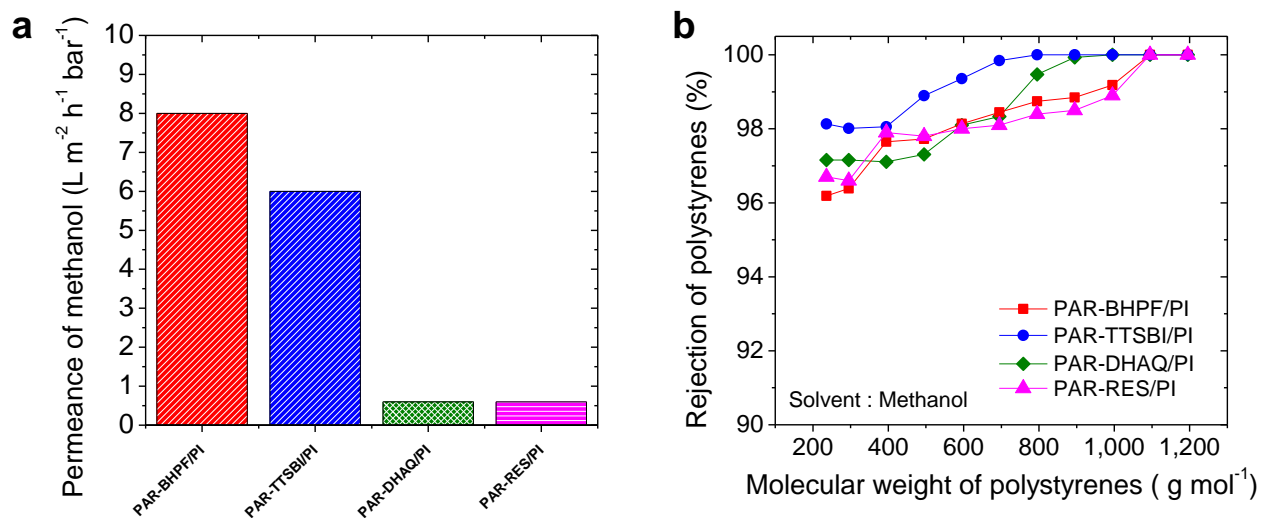




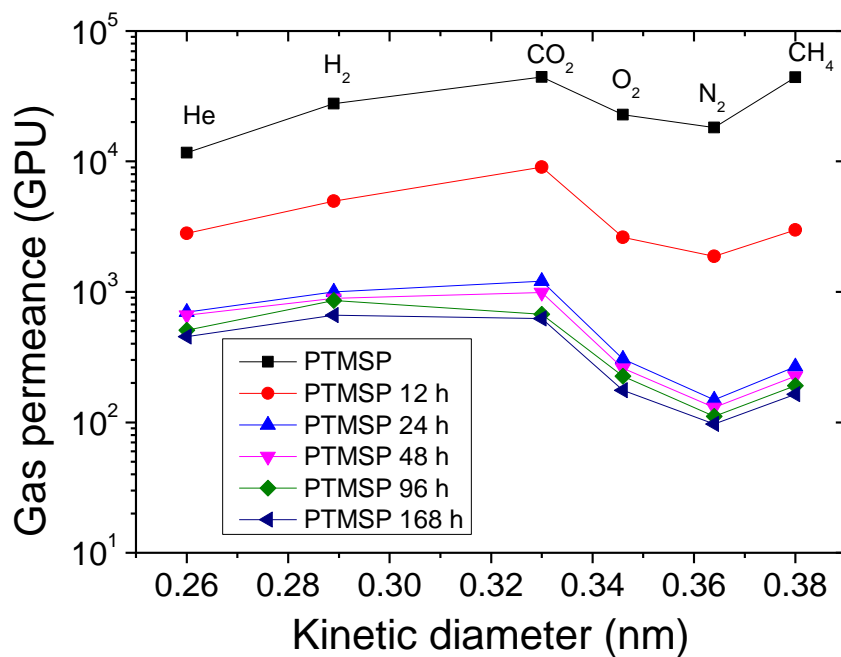
**Supplementary Figure 14. OSN performance of support and ageing of nanofilms on different supports. a,** Rejection versus molecular weight of polystyrene oligomers for crosslinked polyimide support membrane after 24 hours filtration. Nanofiltration of a feed solution comprising polystyrene oligomers dissolved in acetone has been performed at 30 bar and 30 °C. The crosslinked PI support has no selectivity for styrene oligomers. To assess whether the UF support collapses upon curing, the surface of a conditioned UF support with PEG was exposed to an aqueous NaOH solution, followed by a hexane solution and cured in the oven, showing low rejection of styrene oligomers, suggesting no significant collapse occurred during curing. **b,** Pure acetone permeance over time through a PAR-TTSBI/PI nanofilm composite membrane prepared on crosslinked polyimide support, showing ca. 44.9 % permeance decline when steady state is reached. Nanofiltration of pure acetone has been performed at 10 bar and 30 °C. **c,** permeance of different solvents through a free-standing 200nm PAR-BHPF nanofilm on alumina. Nanofiltration of different solvents has been performed at 10 bar and 30 °C using dead end filtration. The cell was depressurized after the end of each 4.5h filtration to change solvent and pressurized again for testing. Methanol filtration was performed at the beginning and at the end of the study, giving the same permeance. No flux decline was observed for the PAR nanofilm on alumina, suggesting that the 45% flux decline in (b) is due to the crosslinked PI support.



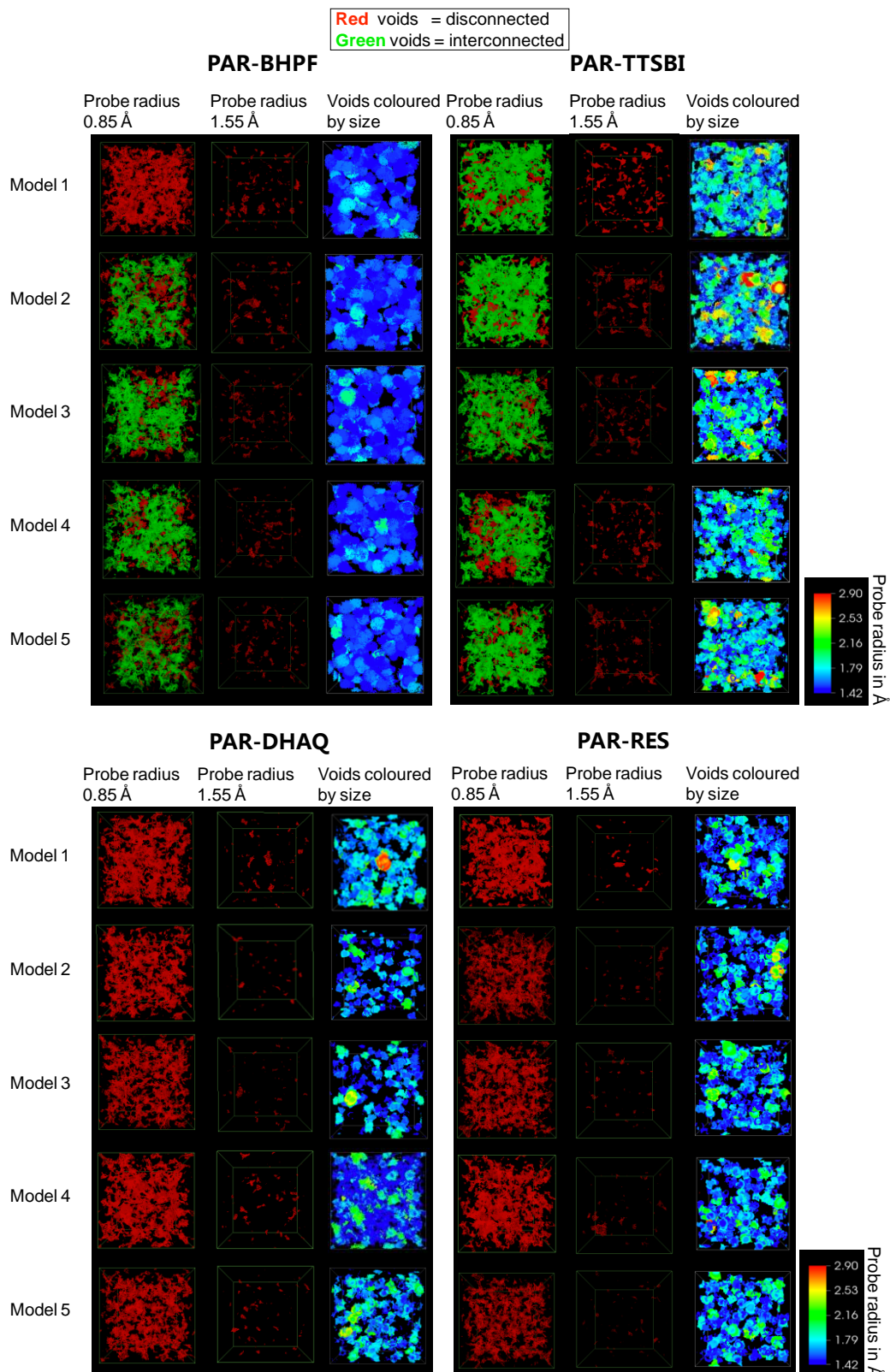
**Supplementary Figure 15. Rejection of dyes.** Photographs of solutions of retentate (R) and permeate (P) containing different dye molecules in methanol after organic solvent nanofiltration. The dyes dissolved in methanol include: Chrysoidine G (CSG,  $249 \text{ g mol}^{-1}$ ), Disperse Red 1 (DR,  $314 \text{ g mol}^{-1}$ ), Crystal violet (CV,  $408 \text{ g mol}^{-1}$ ), and Brilliant blue (BB,  $826 \text{ g mol}^{-1}$ ). Clearly, most of the dye molecules are rejected by the PAR-RES/PI nanofilm composite membrane.



**Supplementary Figure 16. OSN performance of polyarylate nanofilm composite membranes prepared on crosslinked polyimide supports. a,** Permeance of methanol through different PAR/PI nanofilm composite membranes. **b,** MWCO curves of PAR/PI nanofilm composite membranes. Nanofiltration of a feed solution comprising polystyrene oligomers dissolved in methanol has been performed at 30 bar and 30 °C.

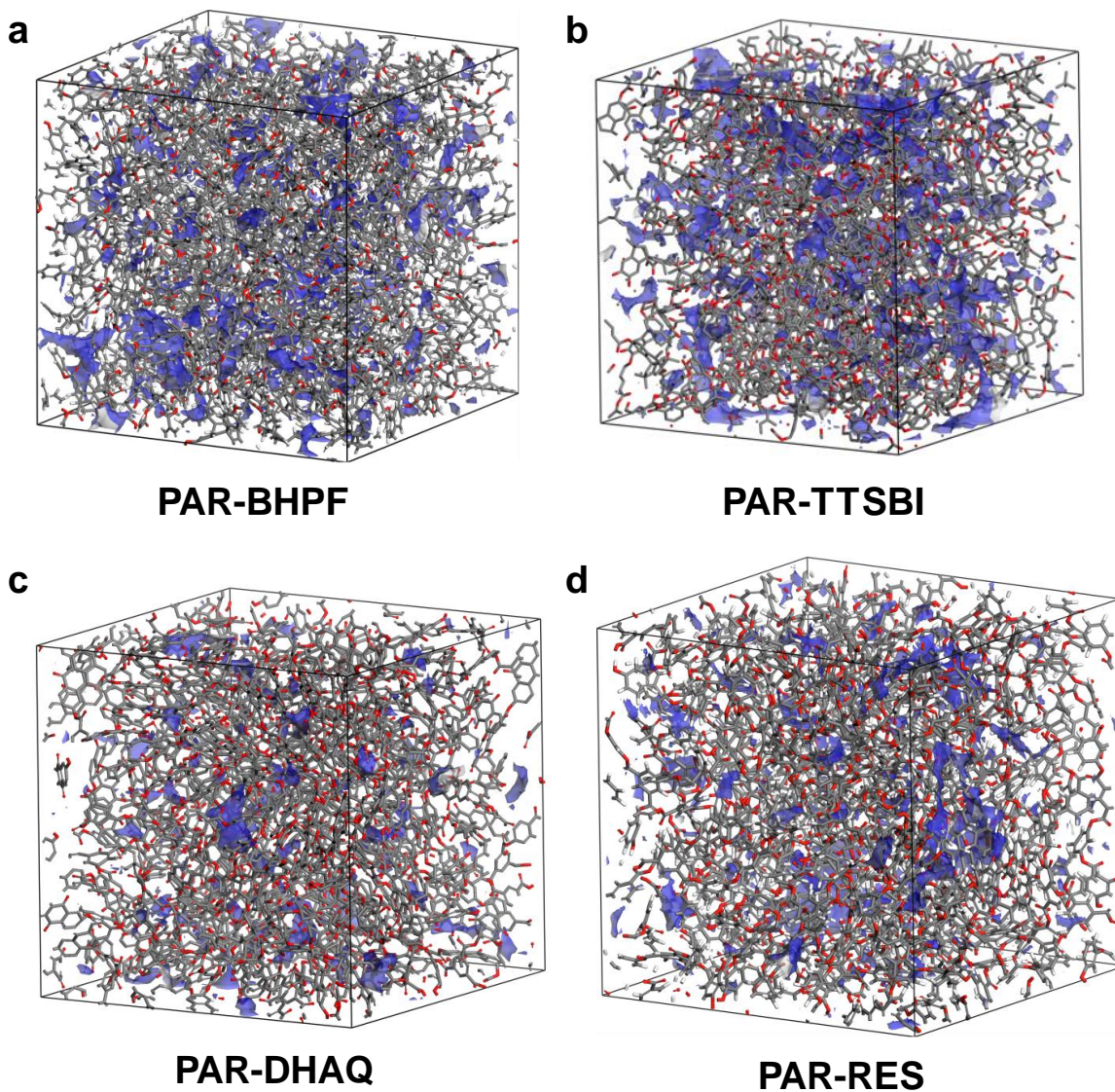


**Supplementary Figure 17. Dynamic change of gas permeance across PTMSP thin film.** A thin layer of PTMSP polymer nanofilm (50 nm) was coated on alumina by spin-coating a 0.5 wt% PTMSP polymer solution in chloroform at 2000 rpm. The cross-sectional SEM images of PTMSP membrane are given in Supplementary Figure 11 (a-b). The polymer membrane was studied in single gas permeation with He, H<sub>2</sub>, CO<sub>2</sub>, O<sub>2</sub>, N<sub>2</sub>, and CH<sub>4</sub>. The polymer was aged continuously for one week under vacuum between gas permeation tests. Gas Permeation Unit (GPU): 1 GPU = 10<sup>-6</sup> cm<sup>3</sup>(S.T.P) s<sup>-1</sup> cm<sup>-2</sup> cmHg<sup>-1</sup>.



**Supplementary Figure 18. Pore structure analysis of the amorphous polymer models.** Left column shows the interconnected (green) and disconnected (red) voids with respect to a probe of 0.85 Å radius- this is the largest size probe that can diffuse across any of the models. These images highlight the difference between the cardo-structured (PAR-BHPF) and spiro-structured (PAR-TTSBI) networks versus the non-contorted, planar PAR-DHAQ and PAR-RES networks. Right column images show the voids coloured with respect to the largest radius probe that can be inserted. Only voids that are larger than a radius of 1.42 Å (the kinetic radius of H<sub>2</sub> gas) are shown. These images illustrate the differences between the contorted and non-contorted systems and demonstrate the homogeneity of the void networks.



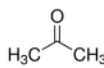
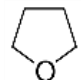
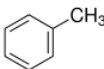


**Supplementary Figure 19. Three-dimensional views of four amorphous cells, each containing a distinct polyarylate network.** Visualisation model carried out in Materials Studio. Blue colour: surface at probe radius of 1 Å diameter. Cell size: 46 × 46 × 46 Å. The boxes show that there are more voids and that there is greater connectivity between voids for the PAR-BHPF and the PAR-TTSBI polymer networks than for the PAR-DHAQ and the PAR-RES polymer networks.

**Supplementary Table 1.** Mechanical properties of smooth spiro-structured PAR-TTSBI free standing nanofilm compared to a smooth polyamide nanofilm prepared via interfacial polymerisation using nanostrands reported in the literature using the same method to determine Elastic modulus.

| Nanofilm                      | Wavelength of the wrinkling pattern, ( $\mu\text{m}$ ) | Thickness of nanofilm $h_f$ (nm) | Elastic modulus of nanofilm $E_f$ (Gpa) |
|-------------------------------|--|----------------------------------|---|
| PAR-TTSBI                     | 3.0  | ~53                              | ~4.8                                    |
| Smooth polyamide <sup>4</sup> | 0.4  | 8.4                              | 2.7                                     |

**Supplementary Table 2.** Properties of solvents used for nanofiltration experiments.

| Name                  | Structure   | Molar volume <sup>a</sup> ( $\text{cm}^3 \text{mol}^{-1}$ ) at 25 °C | Solubility <sup>a</sup> parameter due to dipole force ( $\delta_p$ ) ( $\text{MPa}^{1/2}$ ) at 25 °C | Viscosity <sup>a</sup> (cP) at 25 °C |
|-----------------------|---|--|--|--------------------------------------|
| Methanol (MeOH)       | CH <sub>3</sub> OH  | 40.7   | 12.3   | 0.544                                |
| Acetone               |    | 74.0   | 10.4   | 0.295                                |
| Tetrahydrofuran (THF) |    | 81.7   | 5.7  | 0.480                                |
| Toluene               |  | 106.8  | 1.4  | 0.560                                |

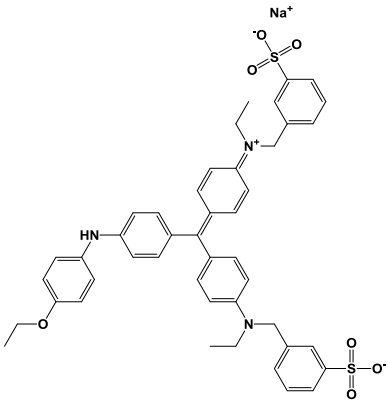
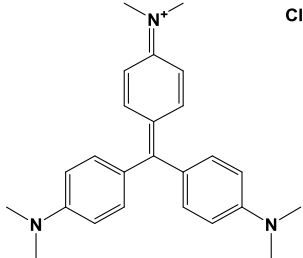
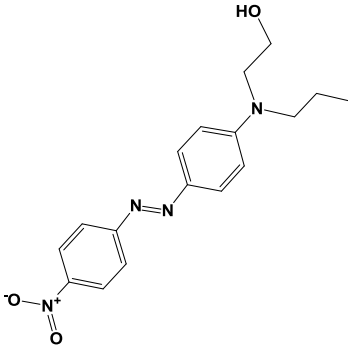
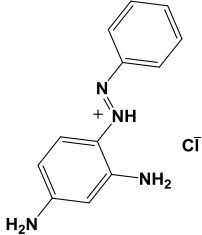
<sup>a</sup> Taken from *Hansen Solubility Parameters: A User's Handbook, 2nd Edition*, Charles M. Hansen, CRC Press, Boca Raton, FL, 2007.

**Supplementary Table 3.** OSN performance of different membranes using  $\alpha$ -methyl styrene dimer as marker for determining rejection in different solvents.

| Nanofilm composite membrane              | Pure MeOH permeance ( $\text{L m}^{-2} \text{h}^{-1} \text{bar}^{-1}$ ) | Styrene dimer rejection (%) | Pure acetone permeance ( $\text{L m}^{-2} \text{h}^{-1} \text{bar}^{-1}$ ) | Styrene dimer rejection (%) | Pure THF permeance ( $\text{L m}^{-2} \text{h}^{-1} \text{bar}^{-1}$ ) | Styrene dimer rejection (%) | Pure toluene permeance ( $\text{L m}^{-2} \text{h}^{-1} \text{bar}^{-1}$ ) | Styrene dimer rejection (%) |
|--|---|-----------------------------|--|-----------------------------|--|-----------------------------|--|-----------------------------|
| PAR-BHPF/PI                              | 8.0   | 96.2                        | 8.4  | 96.7                        | 4.0  | 93.0                        | 0.3  | 90.0                        |
| PAR-TTSBI/PI                             | 6.0   | 98.1                        | 7.0  | 98.8                        | 4.0  | 94.5                        | 2.5  | 91.3                        |
| PAR-DHAQ/PI                              | 0.6   | 97.2                        | 0.2  | 98.0                        | 0.04   | 88.8                        | 0.01   | ND <sup>a</sup>             |
| PAR-RES/PI                               | 0.6   | 96.7                        | 0.4  | 97.8                        | 0.04   | 93.8                        | 0.04   | ND <sup>a</sup>             |
| Freestanding PAR-BHPF (200nm) on alumina | 4.4   | NM <sup>a</sup>             | 4.1  | NM <sup>a</sup>             | 2.8  | NM <sup>a</sup>             | 1.1  | NM <sup>a</sup>             |

<sup>a</sup> not measured (NM), not detectable (ND)

**Supplementary Table 4.** Properties and structure of dyes used as markers for determining rejection in methanol.

| Name                       | Structure   | Charge | Mass (g mol <sup>-1</sup> ) | Volume (Å <sup>3</sup> ) |
|----------------------------|---|--------|-----------------------------|--------------------------|
| <b>Brilliant blue (BB)</b> |    | -      | 825.97                      | 2087.1                   |
| <b>Crystal violet (CV)</b> |    | +      | 407.99                      | 1219.1                   |
| <b>Disperse red 1 (DR)</b> |   | 0      | 314.34                      | 905.6                    |
| <b>Chrysoidine G (CSG)</b> |  | +      | 248.72                      | 737.9                    |



**Supplementary Table 5.** OSN performance of different membranes using dyes as markers for determining rejection in methanol.

| <b>Nanofilm composite membrane</b>       | <b>Pure MeOH permeance (L m<sup>-2</sup> h<sup>-1</sup> bar<sup>-1</sup>)</b> | <b>CSG rejection (%)</b> | <b>DR rejection (%)</b> | <b>CV rejection (%)</b> | <b>BB rejection (%)</b> |
|--|---|--------------------------|-------------------------|-------------------------|-------------------------|
| PAR-BHPF/PI                              | 8.0   | 70.0                     | 90.0                    | 97.0                    | 98.0                    |
| PAR-TTSBI/PI                             | 6.0   | 76.8                     | 91.5                    | 98.7                    | 99.9                    |
| PAR-DHAQ/PI                              | 0.6   | 74.7                     | 90.4                    | 97.7                    | 100                     |
| PAR-RES/PI                               | 0.6   | 93.5                     | 95.4                    | 99.7                    | 99.8                    |
| Freestanding PAR-BHPF (200nm) on alumina | 4.4   | NM <sup>a</sup>          | NM <sup>a</sup>         | NM <sup>a</sup>         | 99.7                    |

<sup>a</sup> (NM) not measured.

**Supplementary Table 6.** Solvent permeance comparison of polyarylate nanofilm composite membranes prepared in this work on crosslinked polyimide PI P84 (XP84) or alumina supports with different polyamide nanofilm composite membranes recently reported by Karan et al<sup>[4]</sup>.

| Support                                     | Nanofilm  | Entry No        | Name               | Morphology      | Thickness (nm)  | Permeance (L m <sup>-2</sup> h <sup>-1</sup> bar <sup>-1</sup> ) |                   |       |         | Reference |
|---|---|-----------------|--------------------|-----------------|-----------------|--|-------------------|-------|---------|-----------|
|   |   |                 |                    |                 |                 | MeOH   | Acetone           | THF   | Toluene |           |
| XP84  | Polyarylate   | 1               | PAR-BHPF           | smooth          | 20              | 8.0  | 8.4               | 4.0   | 0.3     | This work |
|   |   | 2               | PAR-TTSBI          | smooth          | 20              | 6.0  | 7.0               | 4.0   | 2.5     | This work |
|   |   | 3               | PAR-DHAQ           | smooth          | 20              | 0.6  | 0.2               | 0.04  | 0.01    | This work |
|   |   | 4               | PAR-RES            | smooth          | 20              | 0.6  | 0.4               | 0.04  | 0.04    | This work |
|   | Free-standing non-activated polyamide using nanostrands | 5               | MPD-0.1%-3min      | smooth          | 7.5             | 5.1  | NM                | NM    | NM      | [4]       |
|   |   | 6               | MPD-0.1%-10min     | smooth          | 8.4             | 3.8  | NM                | NM    | NM      | [4]       |
|   |   | 7               | PIP-0.1%-10min     | smooth          | 33.2            | 1.4  | 1.09              | NM    | NM      | [4]       |
|   |   | 8               | AMP-0.1%-10min     | smooth          | 14.5            | 4.4  | NM                | NM    | NM      | [4]       |
|   |   | 9               | MPD-3%-1min        | crumpled        | 94 <sup>a</sup> | 7.71   | NM                | NM    | NM      | [4]       |
|   |   | 10              | MPD-4%-1min        | crumpled        | 63 <sup>a</sup> | 4.78   | NM                | NM    | NM      | [4]       |
|   | Free-standing DMF activated polyamide using nanostrands | 11              | MPD-0.1%-3min-ACT  | smooth          | 7.8             | 8.5  | 8.9               | 0.7   | 0.09    | [4]       |
|   |   | 12              | MPD-0.1%-10min-ACT | smooth          | 8.0             | 9.5  | 11.3              | 1.3   | 0.1     | [4]       |
|   |   | 13              | PIP-0.1%-10min-ACT | smooth          | NM              | 1.8  | 1.1               | 0.1   | 0.03    | [4]       |
|   |   | 14              | AMP-0.1%-10min-ACT | smooth          | NM              | 4.2  | 3.3               | 0.3   | 0.3     | [4]       |
|   |   | 15              | MPD-3%-1min-ACT    | crumpled        | 95 <sup>a</sup> | 19.11  | 32.9 <sup>b</sup> | NM    | NM      | [4]       |
|   |   | 16              | MPD-4%-1min-ACT    | crumpled        | 52 <sup>a</sup> | 13.25  | 12.74             | 1.74  | 0.18    | [4]       |
| DMF activated polyamide without nanostrands | 17  | MPD-3%-1min-ACT | crumpled           | NM              | 8.1             | 9.0 <sup>b</sup>   | NM                | NM    | [4]     |           |
| Alumina                                     | Free-standing polyarylate                               | 18              | PAR-BHPF           | smooth          | 200             | 4.4  | 4.1               | 2.8   | 1.1     | This work |
|   | Free-standing non-activated polyamide using nanostrands | 19              | MPD-0.1%-10min     | smooth          | 8.4             | 3.1  | 3.1               | NM    | NM      | [4]       |
|   |   | 20              | MPD-3%-1min        | crumpled        | 94 <sup>a</sup> | 13.73  | 19.34             | 2.59  | 0.08    | [4]       |
|   |   | 21              | MPD-4%-1min        | crumpled        | 63 <sup>a</sup> | 8.9  | 8.3               | 1.02  | 0.29    | [4]       |
|   | Free-standing DMF activated polyamide using nanostrands | 22              | MPD-0.1%-10min-ACT | smooth          | 8.0             | 12.2   | NM                | NM    | NM      | [4]       |
|   |   | 23              | MPD-3%-1min-ACT    | crumpled        | 95 <sup>a</sup> | 52.22  | 49.68             | 18.11 | 3.45    | [4]       |
| 24  |   | MPD-4%-1min-ACT | crumpled           | 52 <sup>a</sup> | 34.12           | 31.16  | 6.02              | 1.31  | [4]     |           |

NM= Not measured. MPD: m-phenylenediamine; PIP: piperazine; AMP: 4-(aminomethyl)piperidine. ACT: activated.

<sup>a</sup> The thickness of the crumpled nanofilms was estimated as the average thickness of the crumpled pattern of the film, not the actual thickness of the film itself and in that case the nanofilms thickness could be in the sub-10nm range.

<sup>b</sup> Acetone permeance for crumpled MPD-3%-1min-ACT nanofilms prepared without nanostrands is 3.6 times lower than MPD-3%-1min-ACT nanofilm composite membranes prepared with a nanostrand layer on the same support (Entries 15 and 17).

Two types of membranes are reported: those utilising crosslinked P84 (XP84) supports, which represent a scalable format (Entries 1-17); and those mounted on alumina discs, which are used to determine isolated nanofilm properties (Entries 18-24). For the composite membranes utilising crosslinked P84 supports, the 20-nm-thick smooth PAR-BHPF nanofilm (Entry 1) gives a MeOH permeance of 8.0 L m<sup>-2</sup> h<sup>-1</sup> bar<sup>-1</sup>, which is about two times higher than smooth polyamide nanofilms made with nanostrands (Entries 5-8; in the range of 1.4-5.1 L m<sup>-2</sup> h<sup>-1</sup> bar<sup>-1</sup>). It is comparable to values for DMF-activated smooth polyamide nanofilms (Entries 11-14; 1.8-9.5 L m<sup>-2</sup> h<sup>-1</sup> bar<sup>-1</sup>), even though the MPD based polyamide nanofilms (Entries 11-12) are less than half the thickness

(8 nm). Polyarylate nanofilm performance becomes even more favourable as solvent polarity decreases, for example in THF and toluene. MPD based polyamide nanofilms with their effective filtration area increased through crumpling exhibit relatively higher permeance for MeOH (Entry 16;  $13.2 \text{ L m}^{-2} \text{ h}^{-1} \text{ bar}^{-1}$ ) and acetone ( $12.7 \text{ L m}^{-2} \text{ h}^{-1} \text{ bar}^{-1}$ ), but their THF permeance is less than half ( $1.74 \text{ L m}^{-2} \text{ h}^{-1} \text{ bar}^{-1}$ ) of that for PAR-BHPF and PAR-TTSBI (Entries 1-2;  $4 \text{ L m}^{-2} \text{ h}^{-1} \text{ bar}^{-1}$ ). Permeance for non-polar toluene through these crumpled polyamide nanofilms (Entry 16;  $0.18 \text{ L m}^{-2} \text{ h}^{-1} \text{ bar}^{-1}$ ) is 10 times lower than that of PAR-TTSBI (Entry 2;  $2.5 \text{ L m}^{-2} \text{ h}^{-1} \text{ bar}^{-1}$ ), even though the effective area of crumpled nanofilms is reported to be 2-4 times higher than equivalent smooth films<sup>4</sup>.

We were unable to prepare free-standing polyarylate nanofilms of sufficient area for liquid filtration tests below 200 nm in thickness, whereas the crumpled MPD based membranes activated with DMF (Entries 23-24) were around 10 nm in thickness - hence their exceptional permeances of around  $50 \text{ L m}^{-2} \text{ h}^{-1} \text{ bar}^{-1}$ .

**Supplementary Table 7.** Parameters derived from experimental and modelling data. For the modelling data the table shows the average over 5 models.

| Parameters   |   | PAR-BHPF        | PAR-TTSBI       | PAR-DHAQ        | PAR-RES         |
|--------------|---|-----------------|-----------------|-----------------|-----------------|
| Experimental | Density PAR-IP (g cm <sup>-3</sup> )  | 1.0327 ± 0.0158 | 1.0366 ± 0.0324 | 1.3207 ± 0.0121 | NM <sup>a</sup> |
|              | Density PAR-MP (g cm <sup>-3</sup> )  | 1.2666 ± 0.0042 | 1.3367 ± 0.0036 | 1.5188 ± 0.0262 | 1.5151 ± 0.0030 |
| Simulation   | Final density at 300K, 1bar (g cm <sup>-3</sup> )                                 | 1.187 ± 0.0030  | 1.213 ± 0.0010  | 1.421 ± 0.0070  | 1.380 ± 0.004   |
|              | Diameter of the largest cavity (Å)  | 5.6 ± 0.1       | 5.6 ± 0.1       | 4.4 ± 0.3       | 4.3 ± 0.2       |
|              | Largest “free” sphere (Å)   | 1.7 ± 0.1       | 1.6 ± 0.1       | 1.3 ± 0.1       | 1.3 ± 0.0       |
|              | Surface area for 1 Å radius probe (m <sup>2</sup> g <sup>-1</sup> )               | 810 ± 8         | 674 ± 39        | 339 ± 32        | 0.0             |
|              | Surface area for 1.55 Å (N <sub>2</sub> ) probe (m <sup>2</sup> g <sup>-1</sup> ) | 102 ± 10        | 74 ± 6          | 18 ± 5          | 0.0             |
| Experimental | Surface area for N <sub>2</sub> via IP (m <sup>2</sup> g <sup>-1</sup> )          | 30.75           | 28.77           | 12.35           | 11.96           |
|              | Surface area for CO <sub>2</sub> via IP (m <sup>2</sup> g <sup>-1</sup> )         | 79.16           | 89.78           | 18.38           | 35.42           |
|              | Surface area for CO <sub>2</sub> via MP (m <sup>2</sup> g <sup>-1</sup> )         | 150.90          | 161.50          | 67.73           | 61.10           |

<sup>a</sup> NM: not measured. Note: we have difficulty in measuring the skeletal density of this sample by helium pycnometry.

**Supplementary Table 8.** Parameters derived from experimental and modelling data. For the modelling data the table shows the average over 5 models. Polymerisation completeness is calculated assuming that all C=O groups reacting is a “complete polymerisation”. For all cases there is essentially one large interconnected network, with one or a few unreacted molecules.

| Polymer   | Percentage polymerisation complete | Polymerisation steps performed | No. of molecules in final model | No. of unreacted COOH groups | No. of unreacted OH groups |
|-----------|------------------------------------|--------------------------------|---------------------------------|------------------------------|----------------------------|
| PAR-BHPF  | 86.7 ± 0.7                         | 317 ± 3                        | 6 ± 2                           | 49 ± 3                       | 49 ± 3                     |
| PAR-TTSBI | 100.0 ± 0.1                        | 402 ± 0                        | 4 ± 1                           | 0 ± 0                        | 402* ± 0                   |
| PAR-DHAQ  | 91.8 ± 1.2                         | 440 ± 6                        | 2 ± 1                           | 41 ± 6                       | 41 ± 6                     |
| PAR-RES   | 98.0 ± 0.4                         | 564 ± 2                        | 1.2 ± 0.4                       | 11.6 ± 2.1                   | 11.6 ± 2.1                 |

\* Contrary to expectation, it was observed that the TTSBI frequently reacted with two trimesoyl chlorides on one side. The PAR-TTSBI systems have many OH functional groups remaining as there were twice the number needed on the original precursor.

## Supplementary References

1. Jeromenok, J., Böhlmann, W., Antonietti, M., & Weber, J., Intrinsically microporous polyesters from betulin – toward renewable materials for gas separation made from birch bark. *Macromol. Rapid Commun.* **32**, 1846-1851 (2011).
2. Chung, J. Y., Lee, J.-H., Beers, K. L., & Stafford, C. M., Stiffness, strength, and ductility of nanoscale thin films and membranes: A combined wrinkling–cracking methodology. *Nano Lett.* **11**, 3361-3365 (2011).
3. Freger, V., Swelling and morphology of the skin layer of polyamide composite membranes: An atomic force microscopy study. *Environmental Science & Technology* **38**, 3168-3175 (2004).
4. Karan, S., Jiang, Z., & Livingston, A. G., Sub-10 nm polyamide nanofilms with ultrafast solvent transport for molecular separation. *Science* **348**, 1347-1351 (2015).